Journal of Remote Sensing
A SCIENCE PARTNER JOURNAL

RESEARCH ARTICLE

Mapping Spatially Seamless Fractional Vegetation Cover over China at a 30-m Resolution and Semimonthly Intervals in 2010–2020 Based on Google Earth Engine

Tian Zhao[1], Xihan Mu[1,2*], Wanjuan Song[3], Yaokai Liu[4], Yun Xie[5,6], Bo Zhong[3], Donghui Xie[1,2], Lingmei Jiang[1,2], and Guangjian Yan[1,2]

[1]State Key Laboratory of Remote Sensing Science, Faculty of Geographical Science, Beijing Normal University, Beijing 100875, China. [2]Beijing Engineering Research Center for Global Land Remote Sensing Products, Faculty of Geographical Science, Beijing Normal University, Beijing 100875, China. [3]State Key Laboratory of Remote Sensing Science, Aerospace Information Research Institute, Chinese Academy of Sciences, Beijing 100101, China. [4]Key Laboratory of Quantitative Remote Sensing Information Technology, Aerospace Information Research Institute, Chinese Academy of Sciences, Beijing 100094, China. [5]State Key Laboratory of Earth Surface Processes and Resource Ecology, Faculty of Geographical Science, Beijing Normal University, Beijing 100875, China. [6]College of Arts and Sciences, Beijing Normal University, Zhuhai 519087, China.

*Address correspondence to: muxihan@bnu.edu.cn

Citation: Zhao T, Mu X, Song W, Liu Y, Xie Y, Zhong B, Xie D, Jiang L, Yan G. Mapping Spatially Seamless Fractional Vegetation Cover over China at a 30-m Resolution and Semimonthly Intervals in 2010–2020 Based on Google Earth Engine. *J. Remote Sens.* 2023;3:Article 0101. https://doi.org/10.34133/remotesensing.0101

Submitted 20 March 2023
Accepted 26 November 2023
Published 19 December 2023

Fractional vegetation cover (FVC) is a critical biophysical parameter that characterizes the status of terrestrial ecosystems. The spatial resolutions of most existing FVC products are still at the kilometer level. However, there is growing demand for FVC products with high spatial and temporal resolutions in remote sensing applications. This study developed an operational method to generate 30-m/15-day FVC products over China. Landsat datasets were employed to generate a continuous normalized difference vegetation index (NDVI) time series based on the Google Earth Engine platform from 2010 to 2020. The NDVI was transformed to FVC using an improved vegetation index (VI)-based mixture model, which quantitatively calculated the pixelwise coefficients to transform the NDVI to FVC. A comparison between the generated FVC, the Global LAnd Surface Satellite (GLASS) FVC, and a global FVC product (GEOV3 FVC) indicated consistent spatial patterns and temporal profiles, with a root mean square deviation (RMSD) value near 0.1 and an R^2 value of approximately 0.8. Direct validation was conducted using ground measurements from croplands at the Huailai site and forests at the Saihanba site. Additionally, validation was performed with the FVC time series data observed at 151 plots in 22 small watersheds. The generated FVC showed a reasonable accuracy (RMSD values of less than 0.10 for the Huailai and Saihanba sites) and temporal trajectories that were similar to the field-measured FVC (RMSD values below 0.1 and R^2 values of approximately 0.9 for most small watersheds). The proposed method outperformed the traditional VI-based mixture model and had the practicability and flexibility to generate the FVC at different resolutions and at a large scale.

Introduction

Fractional vegetation cover (FVC) is usually defined as the areal proportion of the vegetation to the total surface [1]. FVC, which reflects the distribution status and coverage degree of surface vegetation, is widely used in ecological environmental assessments and climate change simulations [2–4]. High-quality FVC products with high spatiotemporal resolutions over large areas are in high demand for soil erosion risk assessments, precision agriculture studies, and urban ecosystem research [5–10].

Until now, the spatial resolutions of most published FVC products were at the kilometer level, which cannot meet the requirements for a spatially refined description of surface vegetation (Table 1) [11]. In recent years, the amount of remotely sensed data with a high spatial resolution at the meter or even submeter level (e.g., Sentinel-2, Gaofen series satellites) has increased. These datasets provide more valuable data sources for the production of finer FVC products. The enhancement of the spatial resolution of FVC products is currently trending [10,12,13]. In addition, observations conducted with a high temporal frequency can record relatively complete cycles of vegetation growth and benefit vegetation phenology research and timely crop monitoring [14,15]. However, there is a lack of fine spatial resolution (30 m or finer) FVC datasets that also

Table 1. Brief summary of the primary existing global or regional FVC datasets

Name	Sensor	Resolution, revisit interval	Spatial range	Temporal range	Algorithm	Reference
Global Monthly Greenness Fraction	AVHRR	0.15°, 30 days	Global	1985–1990	The VI-based mixture model	[20]
POLDER FVC	POLDER	6 km, 10 days	Global	1996–1997, 2003	Neural network	[21,73]
LSA SAF FVC	SEVIRI	3 km, daily/ 10 days	Europe, Africa, South America	2005–current	The decomposition of linear mixed model	[74,75]
TOAVEG FVC	MERIS	0.3 km, 30 days/10 days	Europe	2002–2012	Neural network	[76]
CYCLOPES FVC	SPOT/ VEGETATION	1 km, 10 days	Global	1999–2007	Neural network	[22]
GEOV1/2 FVC	SPOT/ VEGETATION, PROBA-V	1/112°, 10 days	Global	1999–2020	Neural network	[77]
GEOV3 FVC	Sentinel-3/OLCI, PROBA-V	1/3 km, 10 days	Global	2014–current	Neural network	[32]
GLASS FVC	MODIS	500 m, 8 days	Global	2000–2021	Neural network	[30]
TRAGL FVC	MODIS	1 km, 8 days	Global	2000–2014	Gap fraction model	[23]
MuSyQ FVC	MODIS; FY3A/ MERSI; FY3B/ MERSI	1 km, 5 days	China-Asian	2013	The VI-based mixture model	[78]
Landsat FVC	OLI	30 m, seasonal	China	2013–2018	Neural network	[13]
MultiHSVI FVC	EPIC	10 km, daily	Global	2016	The VI-based mixture model	[13]
HJ-1 FVC	MODIS; HJ-1	30 m, 15 days	China	2010	The VI-based mixture model	[11]

have a high temporal frequency, e.g., 30-m resolution products based on Landsat imageries typically have an annual or seasonal frequency [16–18]. Therefore, it is valuable to develop FVC products with higher temporal resolution than those with monthly intervals [19].

Various methods have been established to estimate FVC on a regional or global scale. These methods can be categorized into four types: empirical methods, machine learning approaches, physical models, and vegetation index (VI)-based mixture models [20–23]. Approximately 35% of the relevant studies on FVC employ the VI-based mixture model due to its practicality [24]. However, two endmember parameters of the VI-based mixture model highly influence the accuracy of FVC: the VI values of fully vegetated (Vv) and bare soil pixels (Vs). These parameters are typically acquired through empirical statistics [25,26], whereas it is difficult to obtain accurate endmember VI values, especially for areas lacking fully vegetated pixels and areas lacking bare soil pixels, e.g., semiarid lands and evergreen forests [27]. Although the VI-based mixture model is one of the most prevalent methods for estimating FVC, the challenges of obtaining Vv and Vs values still limit the accuracy of the VI-based mixture model.

A novel algorithm using multiangle data to obtain the two endmember VI values (MultiVI) showed reasonable accuracy in the retrieval of FVC [28]. In contrast to the traditional methods that statistically obtain a limited number of Vv and Vs values (e.g., fixed values for land cover types), the MultiVI method can generate pixelwise endmember VI values. The implementation of MultiVI requires VIs at two large observing angles, which are typically obtained from multiangle datasets with coarse resolutions, such as the products from the Moderate Resolution Imaging Spectroradiometer (MODIS) and the Earth Polychromatic Imaging Camera (EPIC) [13,28]. Generally, the improved VI-based mixture model with Vv and Vs values obtained using the MultiVI method is feasible for generating large-area, high-frequency, and high-resolution FVC products [29]. However, there is still a lack of studies on the application and validation of the MultiVI method for the generation of FVC products with medium or high resolutions.

Therefore, an operational VI-based mixture model was provided to generate fine-spatial-resolution and high-frequency FVC products with good quality over a regional or global scale in this paper. The Vv and Vs values derived from the MODIS data using the MultiVI algorithm were applied to Landsat images to generate 30-m/15-day FVC products from 2010 to 2020 over China. First, the 30-m/15-day normalized difference vegetation index (NDVI) datasets were generated based on a time-series harmonic model with extensive data archives and the computing capabilities of Google Earth Engine (GEE). Subsequently, the two endmember NDVI values of the VI-based mixture model were derived using the MultiVI algorithm to convert the Landsat

NDVI datasets to FVC (hereafter referred to as MultiVI FVC). The accuracy of the MultiVI FVC was validated against the field-measured reference FVC and popular FVC products, i.e., the Global LAnd Surface Satellite (GLASS) FVC and GEOV3 FVC, which were derived from machine learning methods and physical models with reasonable accuracy [30–32]. The *Vv* and *Vs* values acquired from the empirical statistics were also used to generate FVC (hereafter referred to as Statistical FVC) for comparison.

Study Areas and Datasets

Study areas

The study region includes the land region of China (Fig. 1). Figure 1 shows the 30-m fine land cover map of China (GLC_FCS30-2015_V1.0) in 2015, along with the locations of the field measurement sites [33]. Additionally, Fig. 1 illustrates the ecological and geographical zones of China classified based on temperature and moisture conditions (https://www.resdc.cn/data.aspx?DATAID=125).

The field-measured FVC was acquired at sites in Huailai and Saihanba and 151 plots at Chinese soil and water conservation monitoring stations located in 22 small watersheds. The Huailai site (40°20′57″N, 115°47′03″E) is located on a flat plain, covering ~280 km^2. The measurement plots are mainly on agricultural lands, with summer corn as the primary crop, along with a few orchards. The Saihanba site (42°10′41″N, 116°57′52″E) is located at the National Forests Park in Hebei Province, China, where agriculture, pastoralism, and forestry coexist, and the land heterogeneity is relatively stable. The forest in Saihanba is artificial, consisting mainly of larch (*Larix principis-rupprechtii* Mayr.) and birch (*Betula platyphylla* Suk.). The crop types in this area include corn, wheat, and potatoes.

The FVC time series were obtained from Chinese soil and water conservation monitoring stations in 22 small watersheds in 2010. Each station corresponds to a small watershed, and 5 to 7 sampling plots were chosen in each watershed. Figure 1 shows the distribution of the 151 sampling plots, which span most of China and mainly cover the eastern region that is characterized by relatively dense vegetation. These 151 plots are located in diverse climatic and topographical conditions, encompassing various vegetation types, including forests, grasslands, irrigated croplands, and rainfed croplands.

To describe the temporal trajectories of the FVC products from 2010 to 2020, nine BEnchmark Land Multisite ANalysis and Intercomparison of Products (BELMANIP2) sites were used (https://calvalportal.ceos.org/web/olive/site-description). These sites were homogeneous over a 10 km × 10 km area, nearly flat in topography, and nearly free of urban areas and permanent water bodies [34]. Therefore, the BELMANIP2 sites were suitable for validating vegetation parameters. Figure 1 depicts the locations of the nine BELMANIP2 sites. The vegetation biomes in the BELMANIP2 sites include forests, grasslands, and croplands.

Field-measured reference FVC

The sampling plots at the Huailai site were specified on homogeneous land surfaces covered by croplands and orchards and had a plot size of 30 m × 30 m. The field-measured FVC datasets were acquired from digital images taken vertically over the vegetation. The camera was positioned on a long stick and held vertically to capture images of the vegetation (Fig. 2). Images were uniformly taken along two diagonal lines within each sampling plot [35,36]. For the woodlands and orchards, images were taken underneath the crown in a top-down direction to capture the understory vegetation coverage and in an upward direction to quantify the overstory coverage. The FVC was calculated as the weighted sum of the overstory and understory vegetation coverage (f_{up} and f_{down} in Eq. 1). Table 2 provides information on the field-measured FVC datasets.

$$FVC = f_{up} + \left(1 - f_{up}\right) * f_{down} \quad (1)$$

The plots at the Saihanba site were mainly covered by forests and had a plot size of 45 m × 45 m. The FVC time series were measured at the 151 plots with a plot size of 60 m × 60 m at 22 monitoring stations every 15 days in 2010 to acquire the temporal dynamics of vegetation. Approximately nine photos were taken at each plot at the Huailai site, 20 were taken at each plot at the Saihanba site, and five were taken at each time series monitoring plot.

Low-quality images were omitted prior to calculating the FVC. In addition, the homogeneity of the plots was inspected using high-resolution remote sensing images on Google Earth. Plots with significant heterogeneity in their surrounding 90 m × 90 m region (3 × 3 Landsat pixels) were excluded. A shadow-resistant algorithm (SHAR-LABFVC) was implemented to extract the FVC from the digital images of the Huailai and Saihanba sites [37]. This algorithm can eliminate the shadow effect of photos, with a root mean square deviation (RMSD) of approximately 0.025 when validated with visual interpretation and simulated photos. The matching software of the portable photographic instruments (PCOVER) was utilized to calculate FVC for the time series monitoring plots. The use of PCOVER software introduced an absolute error of approximately 5% [38,39].

Since the spatial extent of the field-measured sampling plots was much smaller than the pixels in the GLASS and GEOV3 products, the FVC values measured in a coarse-resolution pixel were arithmetically averaged for the Huailai site. The field-measured FVC at the Saihanba site was upscaled to 500 m using GF-1 data (http://www.sasclouds.com/chinese/home/), considering the spatial heterogeneity of this region. The GF-1 satellite is equipped with four wide field of view (WFV) cameras with a spatial resolution of 16 m. GF-1 WFV images of the Saihanba site collected from June to September 2015 were utilized. An empirical transfer function was employed to convert the GF-1 NDVI map to FVC using Eq. 2 [40–44].

$$FVC = (a * NDVI + b)^n \quad (2)$$

where a, b, and n are the conversion coefficients that transform the NDVI to FVC. The field-measured FVC values, along with their corresponding GF-1 NDVI values at the same pixels, were used to solve the equations through least squares regression. The obtained a, b, and n coefficients were applied to the GF-1 NDVI map to convert it to an FVC map. Subsequently, the GF-1 FVC map was aggregated to a 500-m scale for comparison with the coarse-resolution FVC products (GLASS and GEOV3 FVC).

Satellite datasets

This study employed two types of satellite reflectance datasets to develop FVC products, including the Landsat surface reflectance (SR) product and the MODIS Bidirectional Reflectance

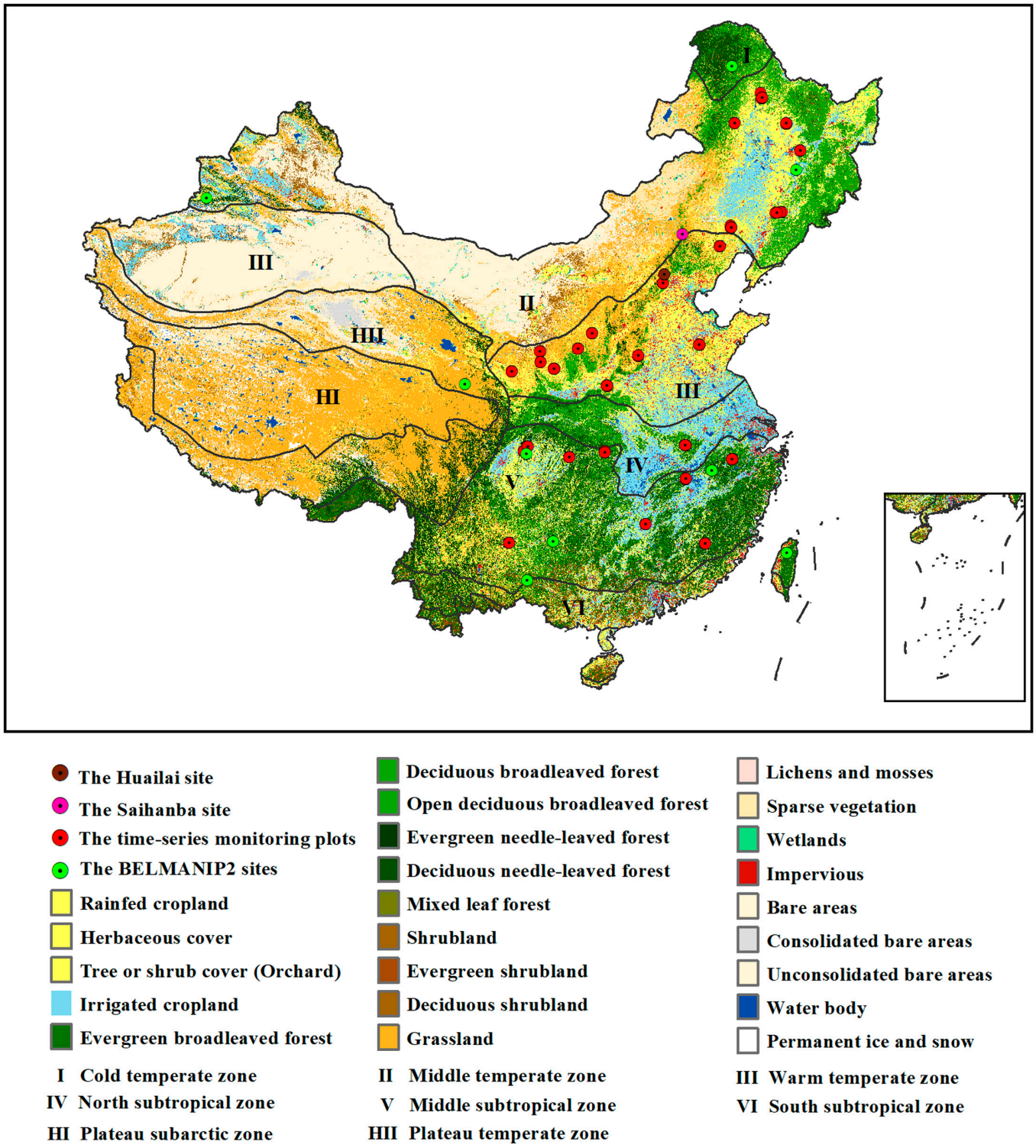

Fig.1. The 30-m land cover map of China. The solid brown circle represents the Huailai site. The solid pink circle indicates the Saihanba site. The solid red circles symbolize the 151 plots of the Chinese soil and water conservation monitoring stations in 22 small watersheds. The solid green circles depict the BELMANIP2 sites. The Chinese ecological and geographical zones are numbered using Roman numerals.

Distribution Factor (BRDF) product. Landsat SR products from the Thematic Mapper (TM), Enhanced Thematic Mapper Plus (ETM+), and Operational Land Imager (OLI) were used to acquire the 30-m/15-day NDVI time series data model. Table 3 illustrates the characteristics and usage of satellite reflectance datasets.

Landsat SR

Landsat Collection 2 SR products, which are conveniently accessible on GEE, were used to calculate the time series NDVI datasets in this study. The Landsat SR images were preprocessed to acquire clear and unified NDVI values from different sensors. The Landsat 5 ETM and Landsat 7 ETM+ SR values for

Fig. 2. Image collection for field-measured reference FVC at the Huailai site.

the red and near-infrared (NIR) bands were adjusted using a linear regression model to be more consistent with the Landsat 8 OLI using the model parameters provided by Roy et al. [45]. The SR datasets have been atmospherically corrected and include a cloud, shadow, water, and snow mask produced using the CFunction of Mask (CFMask) algorithm [46]. All available Landsat images were masked using the corresponding quality bitmask bands to eliminate clouds, cloud shadows, and poor-quality pixels. Figure 3 depicts the number of Landsat scenes utilized in this study for each year.

Terra/aqua MODIS BRDF

The MODIS BRDF product (MCD43A1) and its quality assessment product (MCD43A2) (https://lpdaac.usgs.gov/products/mcd43a1v006/) were applied to generate directional NDVI values as the input parameters of the MultiVI algorithm. The BRDF dataset is produced daily using 16 days of Terra and Aqua MODIS data. MCD43A1 provides the RossThick kernel (volume-scattering kernel), LiSparseR kernel (geometric-optical kernel), and isotropic kernel parameters for the semiempirical linear kernel-driven model (RossThick-LiSparse Reciprocal, RTLSR) [47,48]. It can be used to calculate reflectance in any desired view and illumination direction [46]. The directional NDVI was computed with the red and NIR band kernel parameters. Subsequently, the directional NDVI values were applied to MultiVI to derive the endmember NDVI values of the VI-based mixture model. Using the MCD43A2 quality assessment product, snow, clouds, and low-quality pixels were excluded.

GLASS FVC product

The GLASS FVC has a temporal frequency of 8 days, two sets of spatial resolutions of 0.05° and 500 m (http://www.glass.umd.edu/FVC/MODIS/). In this study, the 500-m GLASS FVC was used to validate the MultiVI FVC. The GLASS FVC was derived using a machine learning approach by building a relationship between MODIS reflectance and FVC. The training samples came from globally preprocessed Landsat images [30,31,49]. The validation result indicated that the RMSD of the GLASS FVC against the field-measured FVC was 0.087, and the correlation coefficient (R^2) was 0.86 [50].

Table 2. Information on the field-measured FVC datasets

Field-measured FVC	Temporal coverage	Number of plots	Land cover type
Huailai FVC	2010, 06/06, 06/19, 06/23, 07/02, 07/10, 07/20, 09/26	35	Orchards, croplands
Saihanba FVC	2015, 06/27, 07/11–07/13, 07/29–07/31, 08/03, 09/12–09/13	33	Forests, croplands, grasslands
Time-series FVC	2010, every 15 days	151	Forests, croplands, grasslands

GEOV3 FCover product

The GEOV FCover is a series of FVC products developed by the Copernicus Program, and it has three major versions. The GEOV3 FVC is the latest version and has been available since 2014 (https://land.copernicus.eu/global/products/fcover). Similar to the previous two versions, the GEOV3 FVC is derived through neural networks (NNTs). The spatial resolution of the product has been improved to 1/3 km, and the temporal frequency is 10 days. An accuracy assessment with field measurements was conducted mainly over crops and resulted in an overall RMSD of 0.21 and a systematic mean overestimation of 0.16 [51]. The GLASS and GEOV3 FVC were used to assess the spatial and temporal consistency of the MultiVI FVC.

Methods

The VI-based mixture model

The VI-based mixture model was used to estimate the continuous 30-m/15-day FVC (Eq. 3) [20]. This model assumes that the reflectance or VI of the mixed pixel is composed of vegetation and soil, with their respective area proportions serving as weighting coefficients [52]. The pixel NDVI value is linearly decomposed by the two endmembers to acquire FVC.

$$FVC = \frac{V - V_s}{V_v - V_s} \tag{3}$$

Here, V is the NDVI value of the mixed pixel; Vv and Vs are the NDVI values of the pure pixel when it is fully vegetated and nonvegetated, respectively.

Retrieval of endmembers

The MultiVI algorithm was utilized to retrieve Vv and Vs for each pixel. The directional NDVI in the VI-based model (Eq. 4) is combined with the gap fraction model (Eq. 5) to establish constrained equations to calculate Vv and Vs (Eqs. 6 and 7) [28,53]:

Table 3. Characteristics and usage of satellite reflectance datasets

Datasets	Satellite sensor	Resolution, revisit interval	Temporal extent	Usage
Landsat5 Surface Reflectance	Landsat 5-TM	30 m, 16 days	2009–2011	Generating 30-m/ 15-day NDVI in 2010
Landsat7 Surface Reflectance	Landsat 7-ETM+	30 m, 16 days	2009–2013	Generating 30-m/ 15-day NDVI in 2010-2014
Landsat8 Surface Reflectance	Landsat 8-OLI	30 m, 16 days	2013–2021	Generating 30-m/ 15-day NDVI in 2013-2020
MCD43A1	Terra/Aqua- MODIS	500 m, daily	2014	Retrieving the two end-member NDVI values of the VI-based mixture model
MCD43A2	Terra/Aqua- MODIS	500 m, daily	2014	Quality assessment for MCD43A1

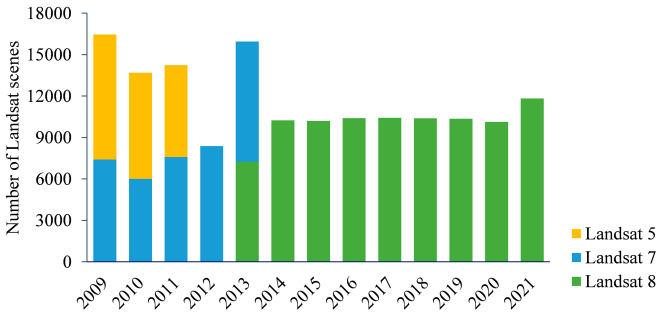

Fig. 3. Number of utilized Landsat scenes for each year in the study area.

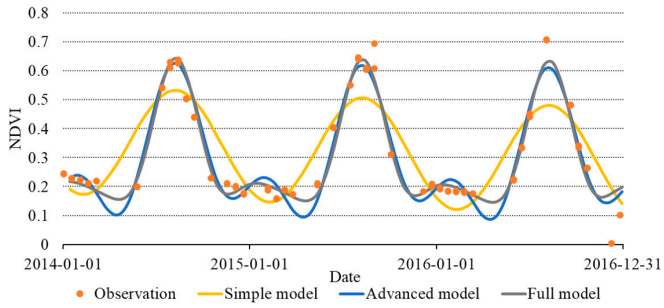

Fig. 4. Simple, advanced, and full models for NDVI based on all available clear Landsat observations between 2014 and 2016 for a crop pixel in northern China (42°34′42″N, 121°54′13″E).

$$F(\theta) = \left(\frac{V(\theta) - V_s}{V_v - V_s}\right)^k \quad (4)$$

$$P(\theta) = e^{-G(\theta)\cdot\Omega\cdot LAI/\cos\theta} \quad (5)$$

where $F(\theta)$ is the directional vegetation cover, which describes the vegetation coverage at view zenith angle (VZA) θ, $V(\theta)$ represents the NDVI value observed at VZA θ, $P(\theta)$is the directional gap fraction, $G(\theta)$ is the mean projection of the unit foliage area [54], Ω is the clumping index, and LAI is the leaf area index. This study employed the nonlinear coefficient k to quantify the FVC with NDVI (Eq. 4), which may mitigate the saturation effect of the NDVI in densely vegetated pixels [26,41,55]. $F(\theta)$ has a complementary relationship with $P(\theta)$ and equals "1- $P(\theta)$"; then, Eqs. 4 and 5 can be combined as:

$$1 - \left(\frac{V(\theta) - V_s}{V_v - V_s}\right)^k = e^{-G(\theta)\cdot\Omega\cdot LAI/\cos\theta} \quad (6)$$

$G(\theta)\cdot\Omega$ is relatively invariant to $\cos\theta$ at large VZAs [27,28,56–58]. Therefore, the estimated equation is established by combining the two observations for VZA at 55° and 60° and by cancelling out the angle-invariant parameters in Eq. 6:

$$\left[1 - \left(\frac{V_i(60°) - V_s}{V_v - V_s}\right)^k\right]^{\cos 60°} = \left[1 - \left(\frac{V_i(55°) - V_s}{V_v - V_s}\right)^k\right]^{\cos 55°} \quad (7)$$

where the subscript "i" stands for the given pixel. The unknown parameters Vv, Vs, and k can be solved utilizing Eq. 7 with angular observations over the whole year for each pixel through the least-squares method. For a given pixel, the directional NDVI at VZAs of 55° and 60°, i.e., $V_i(55^\circ)$ and $V_i(60^\circ)$, was computed and quality-controlled using MCD43A1 and MCD43A2, respectively. The two maps of the endmember values, i.e., Vv and Vs, were generated with a spatial resolution of 500 m. They were then downscaled to a 30-m resolution using the spectral unmixing method [29,59]. The 500-m Vv and Vs in a MODIS pixel are assumed to be the weighted sum of the Vv and Vs of all land cover types in the area of this pixel. The weighted coefficients were represented by the area proportions of land cover types, which were acquired from the 30-m resolution global land cover map (GlobeLand 30, [60]). Then, the 500-m Vv and Vs values could be decomposed to a 30-m scale according to Eq. 8:

$$\begin{cases} V_{v,500} = \sum_{k=1}^{n} f_k V_{v,k} \\ V_{s,500} = \sum_{k=1}^{n} f_k V_{s,k} \end{cases} \quad (8)$$

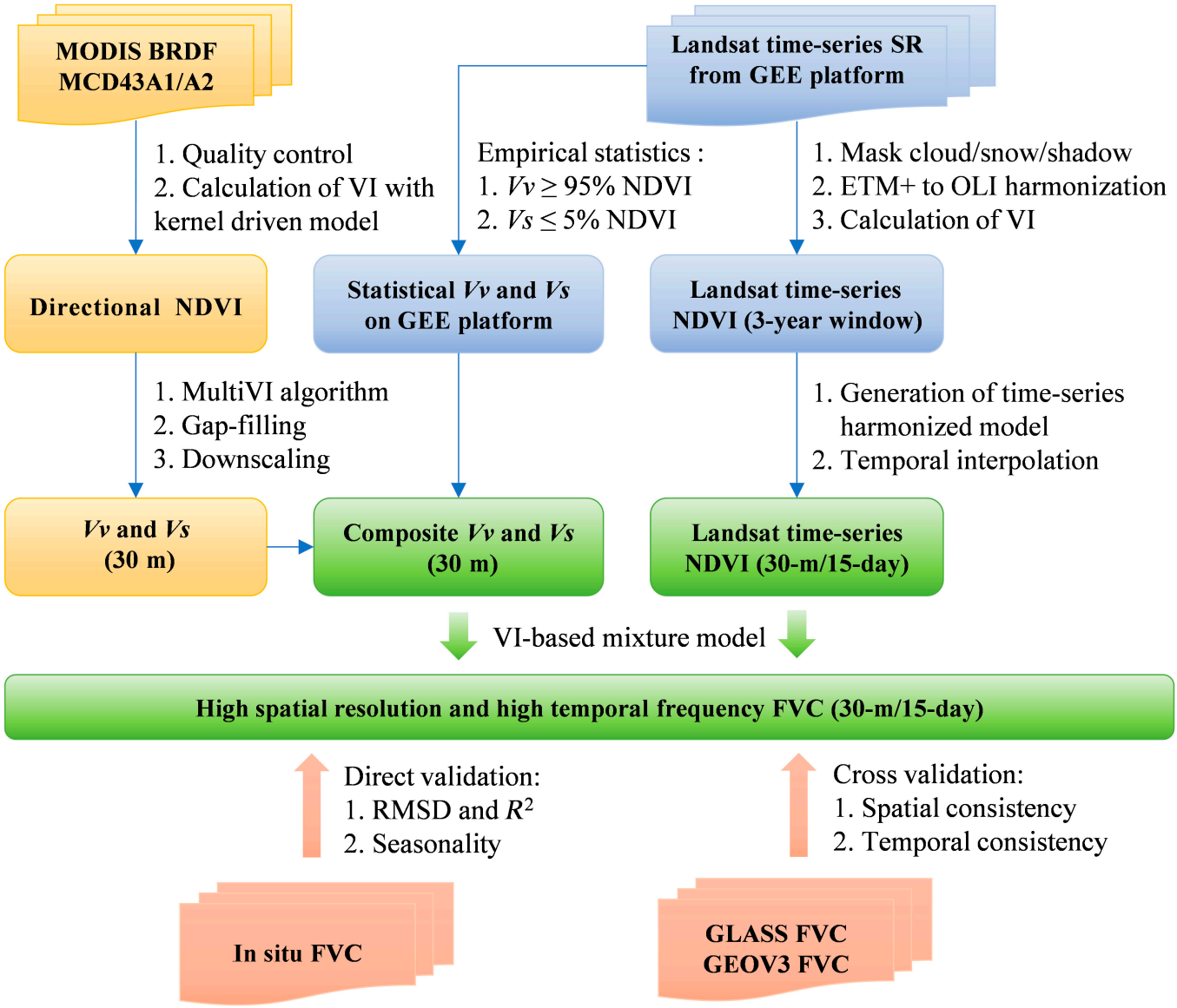

Fig. 5. Flowchart of 30-m/15-day FVC production and validation.

where $V_{v,500}$ and $V_{s,500}$ are the *Vv* and *Vs* for a single MODIS pixel, respectively; f_k is the area proportion of the land cover type k; $V_{v,k}$ and $V_{s,k}$ are the 30-m *Vv* and *Vs* for land cover type *k*; and *n* is the number of land cover types in this 500-m pixel area. To solve the equations, the 3 × 3 500-m pixels surrounding the given MODIS pixel were utilized. The solved $V_{v,k}$ and $V_{s,k}$ were then assigned as the 30-m endmember NDVI values for all the pixels of land cover type *k* within the area of the given MODIS pixel.

However, some pixels had insufficient observations to retrieve reasonable endmember NDVI values due to cloud contamination. The statistical endmember NDVI value was acquired through the time series statistics of Landsat NDVI images on the GEE platform with commonly used statistical criteria. The NDVI values of a given pixel over the whole year were sorted from smallest to largest, and the 5% and 95% accumulative percentages of the NDVI values were *Vs* and *Vv* for the backup algorithm, respectively [60].

Generation of NDVI time series

Three different time series models were applied to estimate the temporally continuous Landsat NDVI values for each pixel. The form of the time series model depended on the number of available clear (hereafter, "clear" refers to the observations that are free of clouds, cloud shadows, and snow) observations and the temporal continuity of the available Landsat images. The time series models adopted could be categorized into three versions, namely, simple, advanced, and full, according to the complexity of the model parameters [61,62].

The simple time series model contained only four parameters, as shown in Eq. 9 [62]:

$$NDVI_{simple}(x) = a_0 + a_1 * \cos\left(\frac{2\pi}{T}x\right) + b_1 * sin\left(\frac{2\pi}{T}x\right) + c_1 * x \quad (9)$$

Here, *x* is the time variable and is represented by the Julian date; $NDVI_{simple}(x)$ denotes the estimated NDVI values at time *x*; *T* represents the cycle period and is set as the number of days per year ($T = 365.25$); a_0 represents the overall value of NDVI; a_1 and b_1 model the intra-annual change caused by phenology and the solar angle variation, respectively; and c_1 models the long-term trend for surface changes. The simple model is effective and

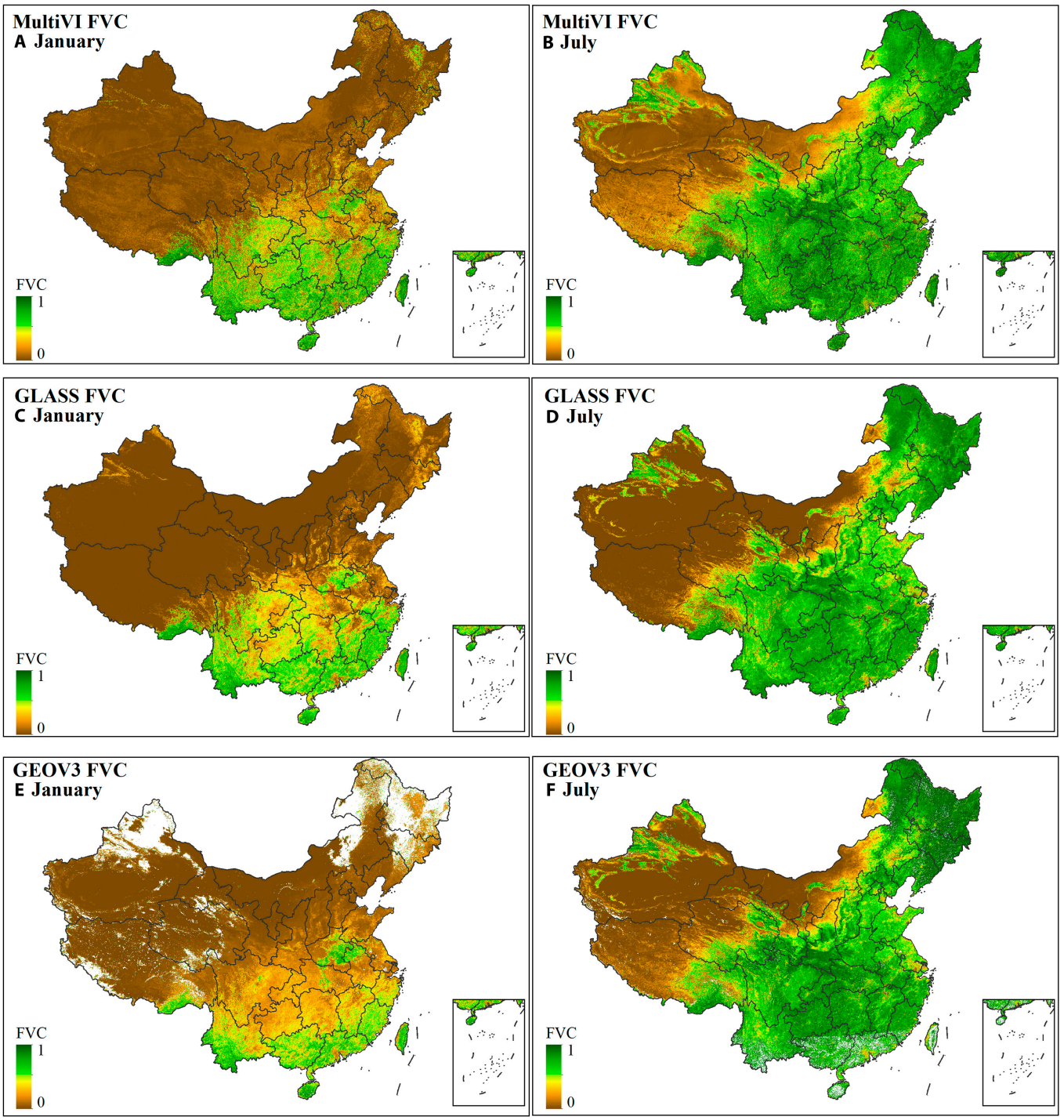

Fig. 6. (A to F) The seasonal spatial distributions of the MultiVI, GLASS, and GEOV3 FVC products in January and July 2015. White areas indicate no data values.

easy to use when interannual changes have a single peak. However, there are places with complex interannual changes that do not follow the simple model. Therefore, the advanced or full model, which can better fit the temporal trajectory, is recommended if more clear observations are available [61]. The advanced and full models are presented in Eqs. 10 and 11, respectively.

$$NDVI_{advanced}(x) = NDVI_{simple}(x) + a_2 * \cos\left(\frac{4\pi}{T}x\right) + b_2 * \sin\left(\frac{4\pi}{T}x\right) \quad (10)$$

$$NDVI_{full}(x) = NDVI_{advanced}(x) + a_3 * \cos\left(\frac{6\pi}{T}x\right) + b_3 * \sin\left(\frac{6\pi}{T}x\right) \quad (11)$$

The advanced model adds two parameters, a_2 and b_2, to the simple model to describe the bimodal intra-annual change. The full model has two more coefficients, a_3 and b_3, based on the advanced model to allow for trimodal intra-annual change. Figure 4 illustrates the NDVI time series values estimated using three different time series models based on all available clear

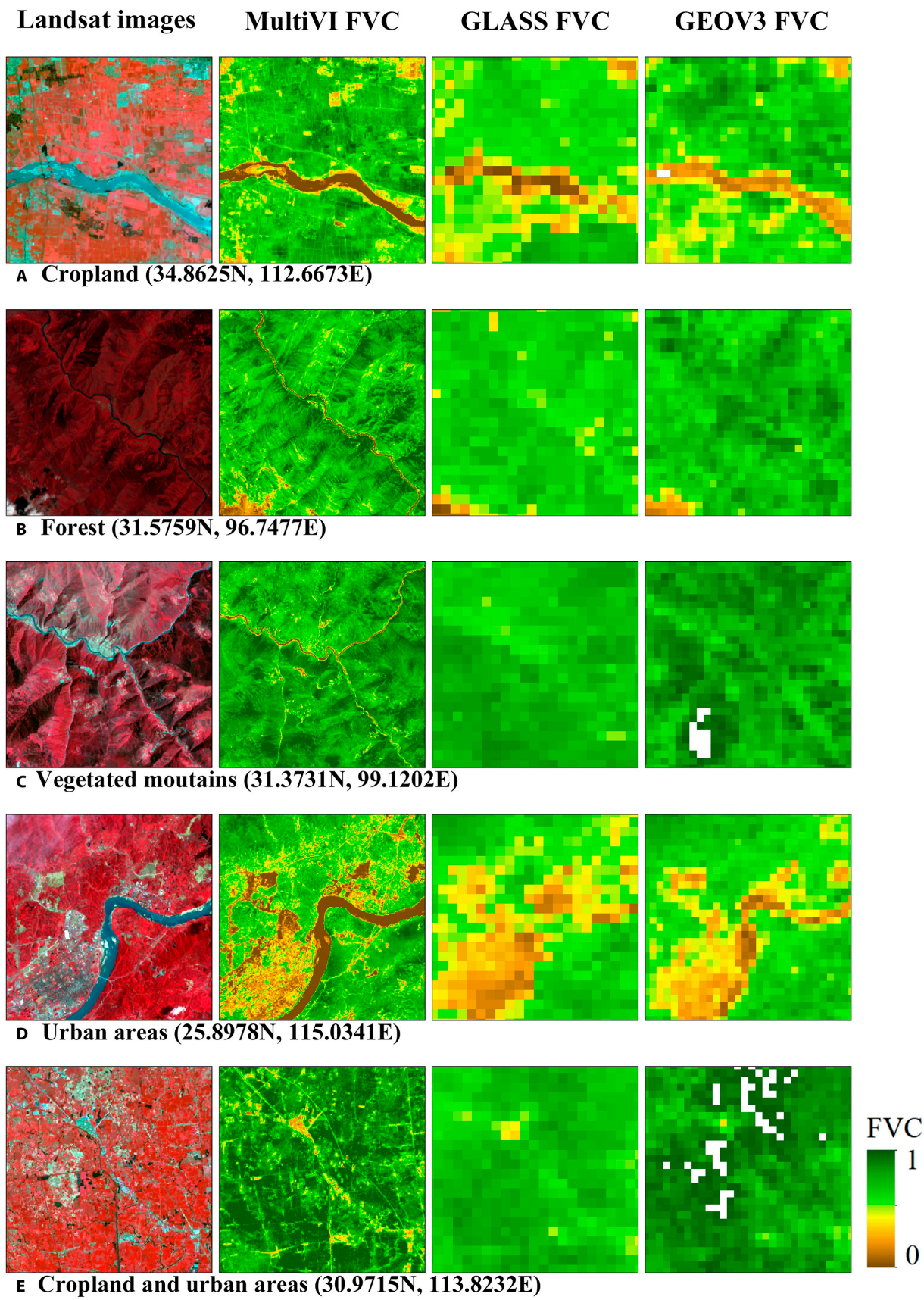

Fig. 7. (A to E) Landsat false-color images and the corresponding MultiVI FVC, GLASS FVC, and GEOV3 FVC for various land covers. Each image represents a spatial extent of 10 km × 10 km. The three FVC products share the same legend.

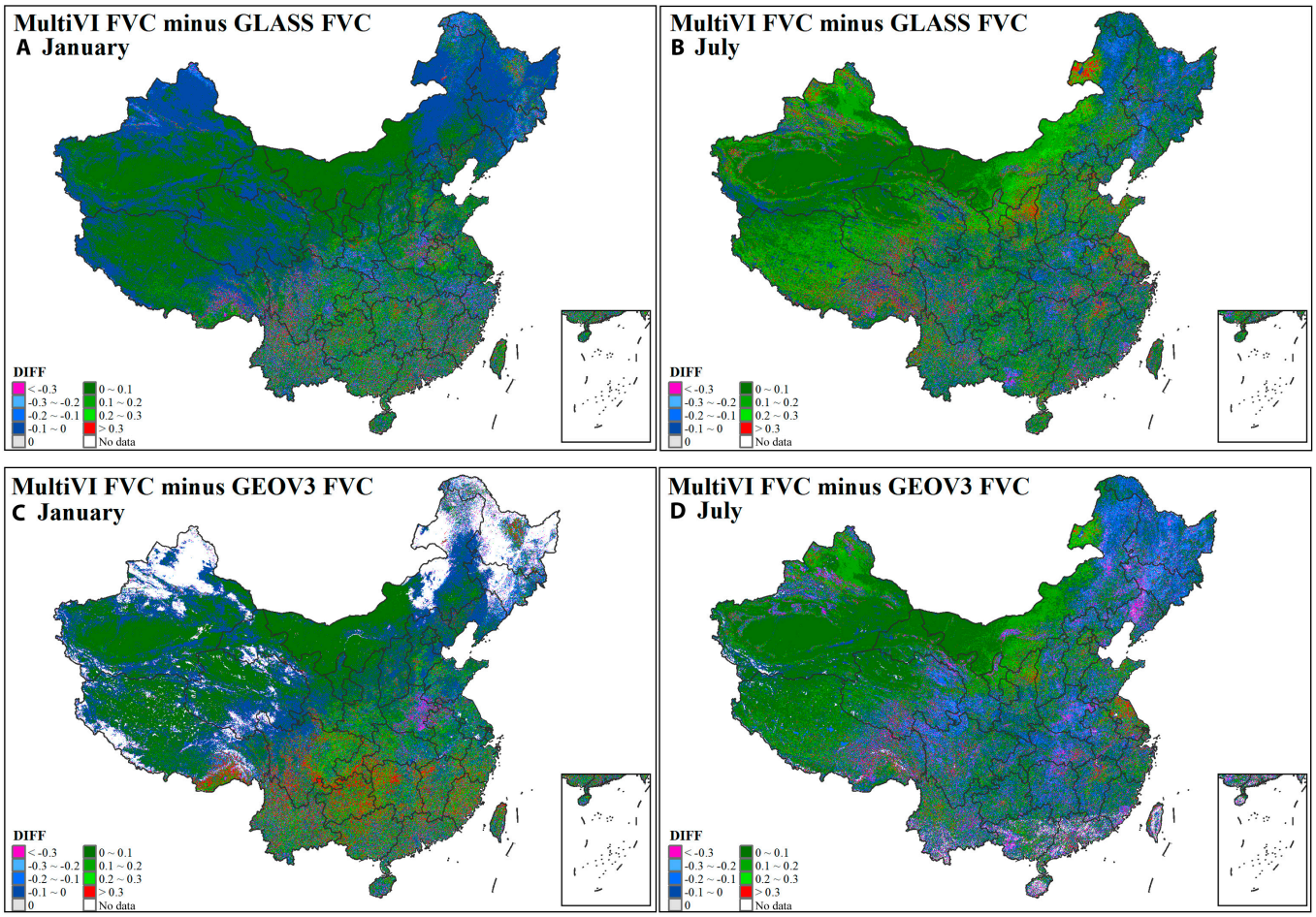

Fig. 8. (A to D) The difference map between the MultiVI FVC, GLASS FVC, and GEOV3 FVC in January and July 2015.

Landsat observations between 2014 and 2016 for a crop pixel in northern China (42°34′42″N, 121°54′13″E). Since the pixel has sufficient clear observations for the full model estimation, the full model shows a more consistent temporal curve with the observations (Fig. 4).

Previous studies suggested that the total number of clear observations should be three times greater than the model coefficients to acquire a robust and accurate time series model [61,62]. This criterion was followed in this study. Applying excessive observations of a long period would introduce long-term trends spanning multiple years into the temporal trajectories of the given year. To ensure the accuracy of fitting and obtain enough clear observations, the Landsat SR data from the year before the given year to the year after that were adopted to establish the time series model. The simple harmonic model was used if the total number of clear observations in the 3 years was greater than or equal to 12 and less than 18 (12 to 17). Otherwise, the advanced model was used if the total number of clear reflectance was greater than or equal to 18 but less than 24 (18 to 23). The full model was applied if the total number of clear observations was greater than or equal to 24 (>24). An excessively large temporal gap between adjacent observation data can cause overfitting problems in the advanced and full models, as the additional coefficients induce extra freedom in the time series model [61]. Therefore, the temporal continuity of the clear observations was also used as one of the constraints when choosing the appropriate time series model. If any large gap (>44 days) existed in the clear observation time series, a simple model was utilized. Most pixels had enough clear observations to establish a suitable time series model. For the pixels that lacked useful data, the mean NDVI values of neighboring spatial or temporal pixels were used to fill the gaps.

Mapping 30-m/15-day FVC in China

The MultiVI FVC products covered the land region of China from 2010 to 2020, with spatial completeness and temporal continuity. The processing steps included the derivation of the *Vv* and *Vs* composite, generation of Landsat time series 30-m/15-day NDVI, calculation of FVC, and validation (Fig. 5).

Assessment and validation

Validation against field measurements and statistical FVC

The field-measured FVC in the Huailai and Saihanba sites was utilized to assess the MultiVI FVC, Statistical FVC, GLASS FVC, and GEOV3 FVC. The Statistical FVC was calculated using the VI-based mixture model in a traditional way. The NDVI values used for the calculation were the same as those used for the MultiVI FVC. The endmember NDVI values were acquired through empirical statistics. *Vv* and *Vs* were extracted from the accumulative maximum and minimum of a 3-year time series dataset, respectively, within a neighborhood centered at the given pixel [27].

To reduce the error caused by the geo-location bias, the MultiVI FVC and Statistical FVC values in 3 × 3 pixels around a measured plot were averaged for comparison with the field-measured FVC,

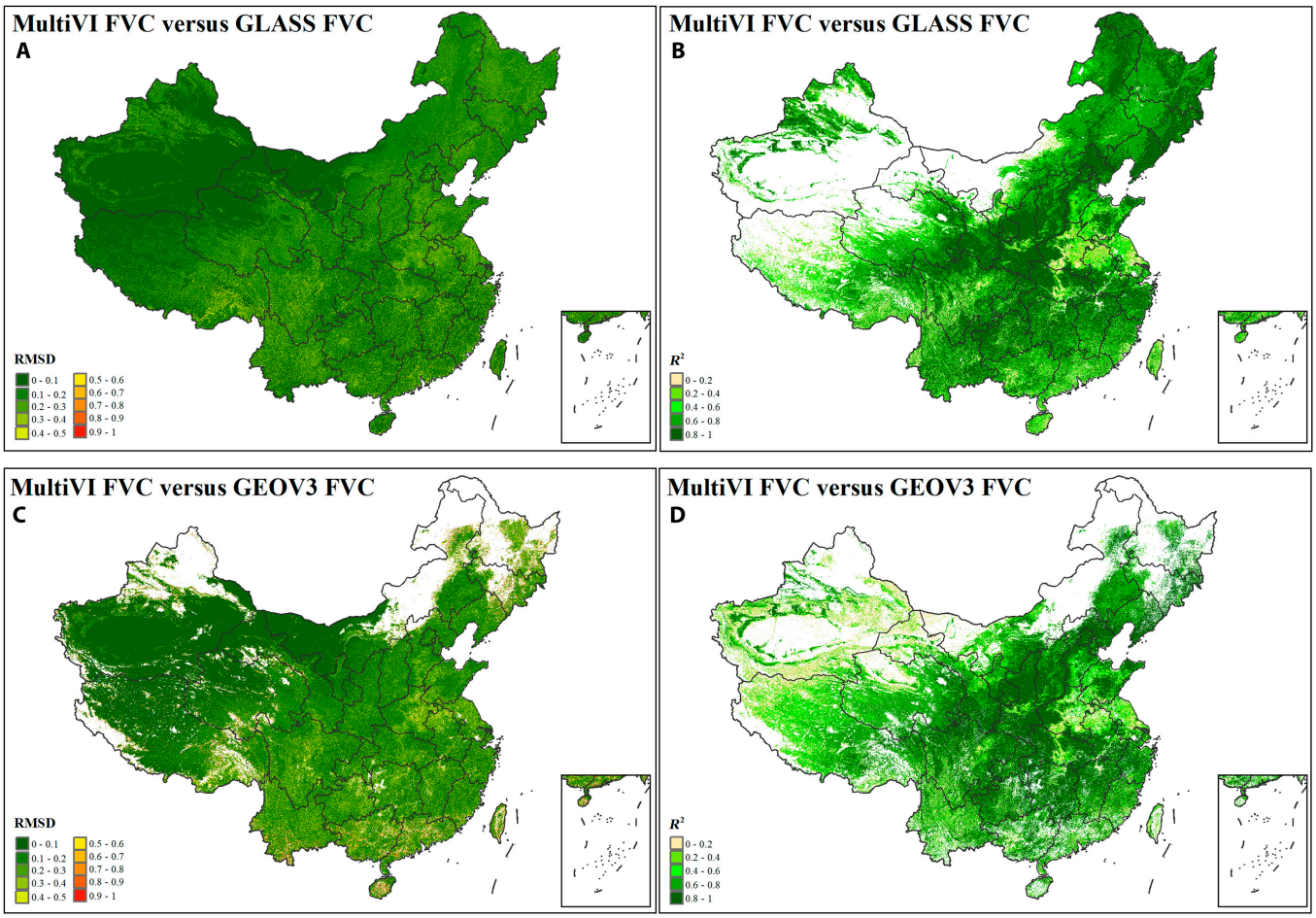

Fig. 9. (A to D) The maps of R^2 and RMSD between the MultiVI FVC, GLASS FVC, and GEOV3 FVC in 2015.

as suggested by Weiss et al. [63]. The correlation coefficient (R^2) was used to indicate the relationship between the field-measured FVC and the validated FVC, and the RMSD was calculated to assess the accuracy.

The FVC observed at the 151 plots around the Chinese soil and water conservation monitoring stations in the 22 small watersheds was not originally designed for the validation of remotely sensed products. Therefore, the FVC time series was mainly used to validate the temporal profiles of the MultiVI FVC, considering the small number of photos for the plot (only five photographs for each plot in half a month; see the "Field-measured reference FVC" section) and the heterogeneity of the sites. The statistical metrics used for comparison were R^2 and RMSD. Moreover, the average bias between the estimated FVC (the MultiVI FVC and Statistical FVC) and the field-measured FVC were calculated for each ecological and geographical zone across the 24 semimonthly time phases.

Intercomparison

The MultiVI FVC was validated using published FVC products whose accuracy has been assessed. The MultiVI FVC and the GEOV3 FVC were resampled to 500 m by averaging the pixel values within each 500-m pixel. Monthly mean FVC values in 2015 were calculated for all three FVC products. The missing pixels were excluded, and only the valid pixels of all three products within the same period were compared. To further evaluate the consistency between the MultiVI FVC and other FVC products, statistical metrics, including the difference (DIFF), R^2, and RMSD, were calculated to assess the agreement between the FVC products for each pixel.

To compare the temporal consistency, the FVC time series values from 2010 to 2020 were extracted from these FVC products at nine BELMANIP2 sites representing major vegetation biomes. The metrics R^2 and RMSD were calculated to quantify the similarity and discrepancy between the temporal trajectories of the three FVC products.

Results

Spatial consistency

Figure 6 shows the monthly maps of the MultiVI FVC, GLASS FVC, and GEOV3 FVC products in January and July 2015. The white areas indicate missing values. The GEOV3 FVC product had many missing values, especially in winter and high-latitude zones, while missing values did not exist in the MultiVI FVC and the GLASS FVC. Since the time series harmonic model was used to retrieve a spatially and temporally continuous NDVI dataset, the MultiVI FVC derived from it exhibited good spatiotemporal completeness. These three FVC products were generally consistent in terms of spatial patterns. The FVC showed a trend of higher values in the southeast and lower values in the northwest, which was consistent with the spatial distribution of precipitation. In January, high FVC values were mainly concentrated in the tropical and subtropical evergreen forests around

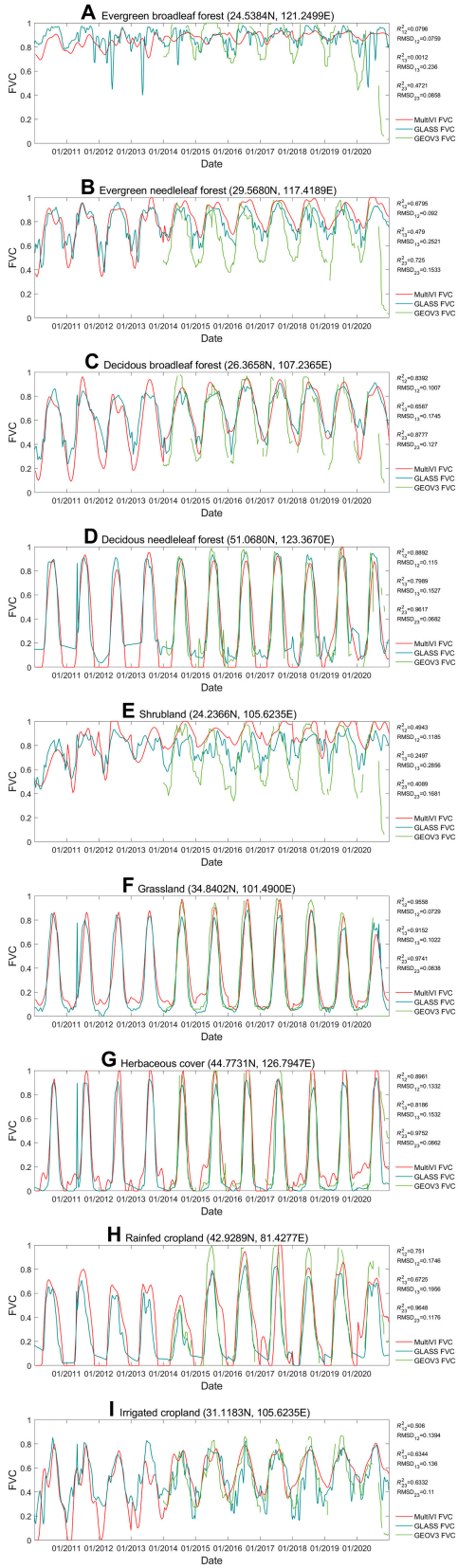

Fig. 10. (A to I) Time-series comparison of the MultiVI FVC, GLASS FVC, and GEOV3 FVC from 2010 to 2020 for nine BELMANIP2 sites with different vegetation types. The R^2 and RMSD values are also shown, and a subscript of "12" represents the MultiVI FVC and GLASS FVC, a subscript of "13" indicates the MultiVI FVC and GEOV3 FVC, and a subscript of "23" depicts the GLASS FVC and GEOV3 FVC.

Southwest China, while the grasslands in northeastern China had very low FVC values. In summer, the FVC values of the deciduous forests in the north increased. Furthermore, the FVC values of the three FVC products were low year-round over the Qinghai–Tibet Plateau and the sparse lands of Xinjiang Province in northwestern China, where the dominant biomes are montane grassland and desert scrubland, respectively. The spatial patterns of the three FVC products were consistent with the ecological and climatic conditions of China.

Figure 7 illustrates the Landsat images under different land cover conditions, as well as the MultiVI FVC, GLASS FVC, and GEOV3 FVC. The MultiVI FVC displayed more distinct spatial details than the coarse-resolution FVC products due to its higher resolution.

Figure 8 shows the monthly difference between the MultiVI FVC and the other two FVC products for January and July 2015. The difference between the MultiVI FVC and the other two FVC products was generally ±0.1 in most areas of China. High discrepancies appeared in irrigated cropland regions, especially in the two-harvest-per-year rice crop area of southeastern China. The MultiVI FVC values were slightly higher than the GLASS FVC values over the grasslands in northern China and lower than those over the deciduous forests in northeastern China (Fig. 8A and B). The GEOV3 FVC values were significantly higher than the MultiVI FVC values over the evergreen region in southwestern China during summer and lower during winter (Fig. 8C and D). This indicated that GEOV3 had a distinct seasonal variation for the evergreen broadleaf forests in southwestern China, while the seasonality of the MultiVI FVC and GLASS FVC was more stable in that region.

Temporal consistency

Figure 9A and C shows that the RMSD between the MultiVI FVC and the other FVC products was close to 0.1 in western, sparsely vegetated areas and did not exceed 0.2 in most areas. There was relatively low accuracy for the dense vegetation in the south, especially in the evergreen forests and near the missing pixels of the GEOV3 FVC. Figure 9B and D shows that the R^2 maps present prominent strong correlations (0.8 to 1) between the MultiVI FVC and the two other products for most of China. Weak correlations (0 to 0.2) were observed in the desert regions of northwest China and the Qinghai–Tibet Plateau between the MultiVI FVC and the GEOV3 FVC, where the FVC values were consistently low (0.1) throughout the year. The lowest R^2 values appeared mainly in flooded rice fields in eastern China. There were large areas of no data pixels in the R^2 map due to a large amount of zero values of the GLASS FVC in the western grassland regions and missing pixels of the GEOV3 FVC.

Figure 10 illustrates the temporal profiles of the MultiVI FVC, GLASS FVC, and GEOV3 FVC over nine BELMANIP2 sites, along with the R^2 and RMSD values between these profiles. Since the GEOV3 FVC began in 2014, their missing periods were not presented. The MultiVI FVC and GLASS FVC showed good continuity in their time profiles, while the GEOV3 FVC had many missing values. The MultiVI FVC demonstrate lower RMSD and higher R^2 values when compared with the GLASS FVC than with the GEOV3 FVC. The RMSD between the MultiVI FVC and the GLASS FVC was below 0.15 at most sites, except for the rainfed cropland site (Fig. 10H).

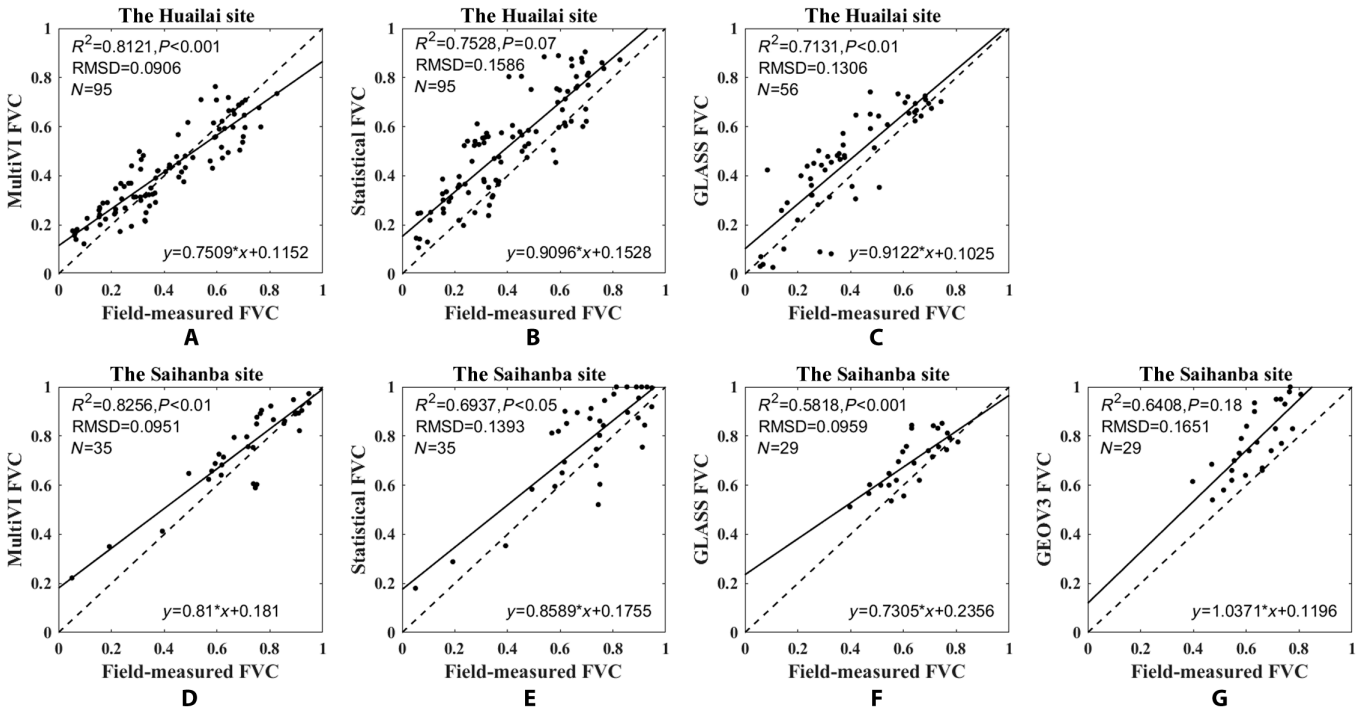

Fig. 11. (A to G) Scatterplots of the FVC products versus the field-measured reference FVC. The R^2 and RMSD values are also shown. *N* is the number of samples for each case.

Figure 10A and B illustrates that the GEOV3 FVC exhibits a significantly higher seasonality than the MultiVI FVC and GLASS FVC at the two evergreen sites. The MultiVI FVC had smoother temporal profiles at these sites, leading to lower R^2 values when compared with the other FVC products. However, the RMSD between the MultiVI FVC and the GLASS FVC at these sites remained reasonable, measuring below 0.1. Figure 10D shows that the MultiVI FVC was zero at the deciduous needleleaf forest site during winter, while the other two products had higher values. This discrepancy was also observed in the rainfed cropland, as shown in Fig. 10H. For the shrubland site, Fig. 10E demonstrates that the GEOV3 FVC showed a wider range of seasonal variations, which contributed to lower correlation and a higher RMSD compared to the other FVC products. At the grassland and herbaceous cover sites (Fig. 10F and G), the temporal profiles of the three products were consistent throughout their trajectories, with R^2 values above 0.8 and RMSD values below 0.16. During the nongrowing season at these sites, the MultiVI FVC values were slightly higher than the values of the other two products.

Direct validation

Figure 11 depicts scatterplots of the FVC products versus the field-measured FVC at the Huailai site (Fig. 10A to C) and the Saihanba site (Fig. 10D to G). The majority of the points in Fig. 10C were above the 1:1 line, indicating that the GLASS FVC values were higher than the field-measured FVC. The MultiVI FVC had slightly better accuracy when compared to the field-measured FVC (RMSD = 0.0906) than the Statistical FVC (RMSD = 0.1586) and the GLASS FVC (RMSD = 0.1306). The correlation between the MultiVI FVC and the field-measured FVC (R^2 = 0.8121) was also superior to the correlation between the Statistical FVC and the field-measured FVC (R^2 = 0.7528), as well as better than the correlation between the GLASS FVC and the field-measured FVC (R^2 = 0.7131).

Figure 11D shows that the accuracy of the MultiVI FVC (RMSD = 0.0951) was close to that of the GLASS FVC (RMSD = 0.0959) yet superior to that of the Statistical FVC (RMSD = 0.1393) and the GEOV3 FVC (RMSD = 0.1651). The majority of the points in Fig. 11G were above the 1:1 line, indicating that GEOV3 overestimated the values compared to the field-measured FVC. Figure 11E shows that several Statistical FVC values were saturated, indicating that the *Vv* from the empirical statistics method was probably underestimated.

Figure 12 depicts a comparison of the field-measured FVC with the MultiVI FVC and Statistical FVC for the 24 temporal phases in 2010 over the 151 plots in 22 small watersheds. The FVC time series were categorized into 12 types based on the vegetation type and topography. The field-measured FVC, MultiVI FVC, and Statistical FVC were compared by calculating the average values for all sites of each type. The R^2 and RMSD values between the field-measured FVC and MultiVI FVC (R^2_M and $RMSD_M$), as well as between the field-measured FVC and Statistical FVC (R^2_S and $RMSD_S$), are also shown. The vegetation phenologies and temporal patterns of the field-measured FVC and MultiVI FVC showed good agreement, with $RMSD_M$ values below 0.1 and R^2_M values reaching 0.9 for most vegetation types. The MultiVI FVC demonstrated significantly higher accuracy than did the Statistical FVC, with $RMSD_M$ values below those of the $RMSD_S$ by up to 0.17 (Fig. 12F). Deviations existed between the field-measured FVC and MultiVI FVC for different vegetation types. For the forest sites in Fig. 12A and B, the MultiVI FVC values were slightly lower than the field-measured FVC in the nongrowing season (winter), with $RMSD_M$ values below 0.1. For the moderate coverage grassland sites in Fig. 12E, the MultiVI FVC values were underestimated compared to the field-measured FVC from January to March, with the highest RMSD value (0.167) among the 12 vegetation types. For the sparse grassland sites in Fig. 12F, the MultiVI FVC and Statistical FVC were both overestimated

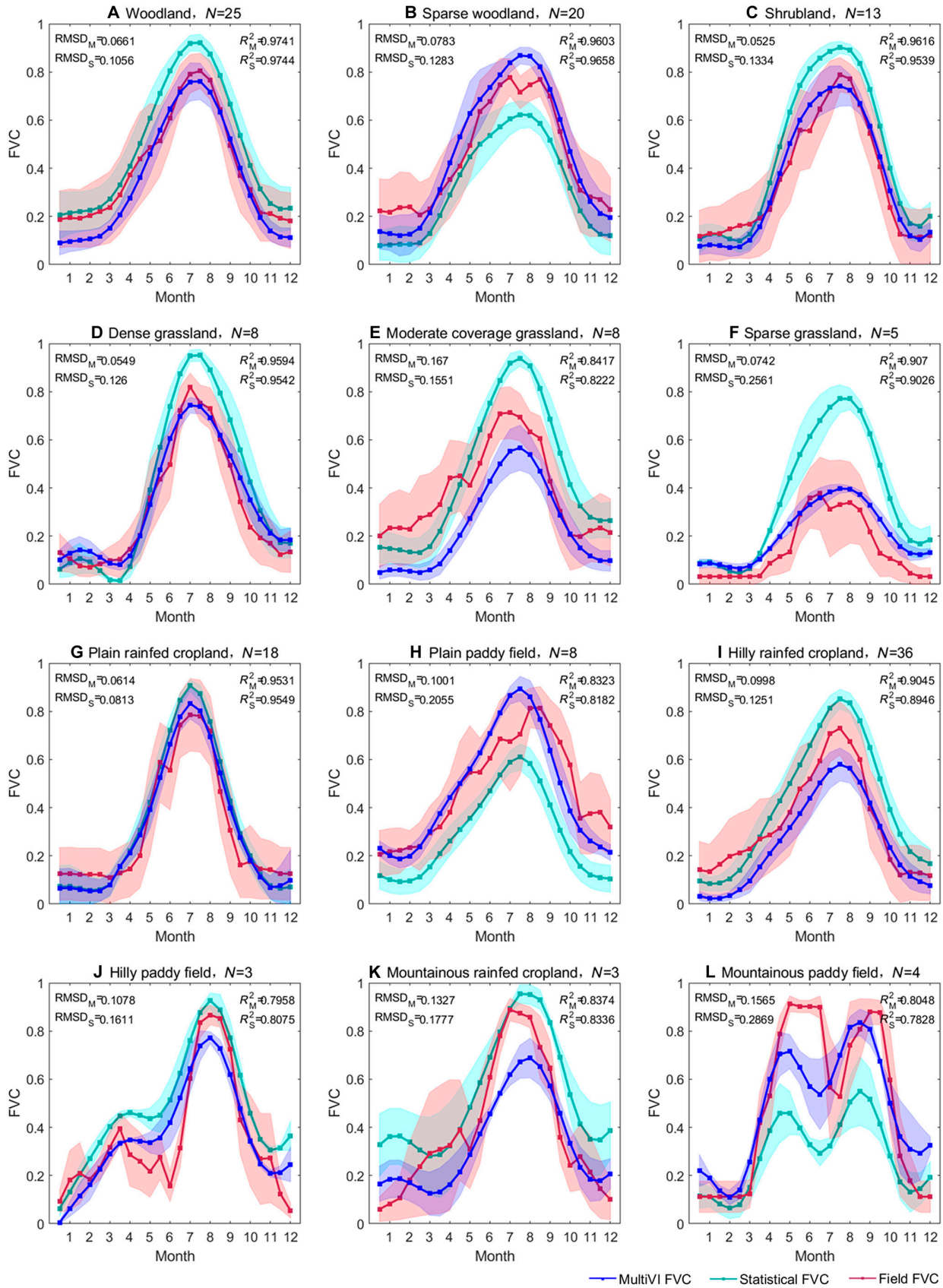

Fig. 12. (A to L) Time series of the MultiVI FVC, Statistical FVC, and field-measured FVC over the time series FVC monitoring plots for the 12 vegetation types in 2010. The width of the shading represents ±1 standard deviation. The R^2 and RMSD values are also shown, the "M" subscript represents the MultiVI FVC, and the "S" subscript indicates the Statistical FVC.

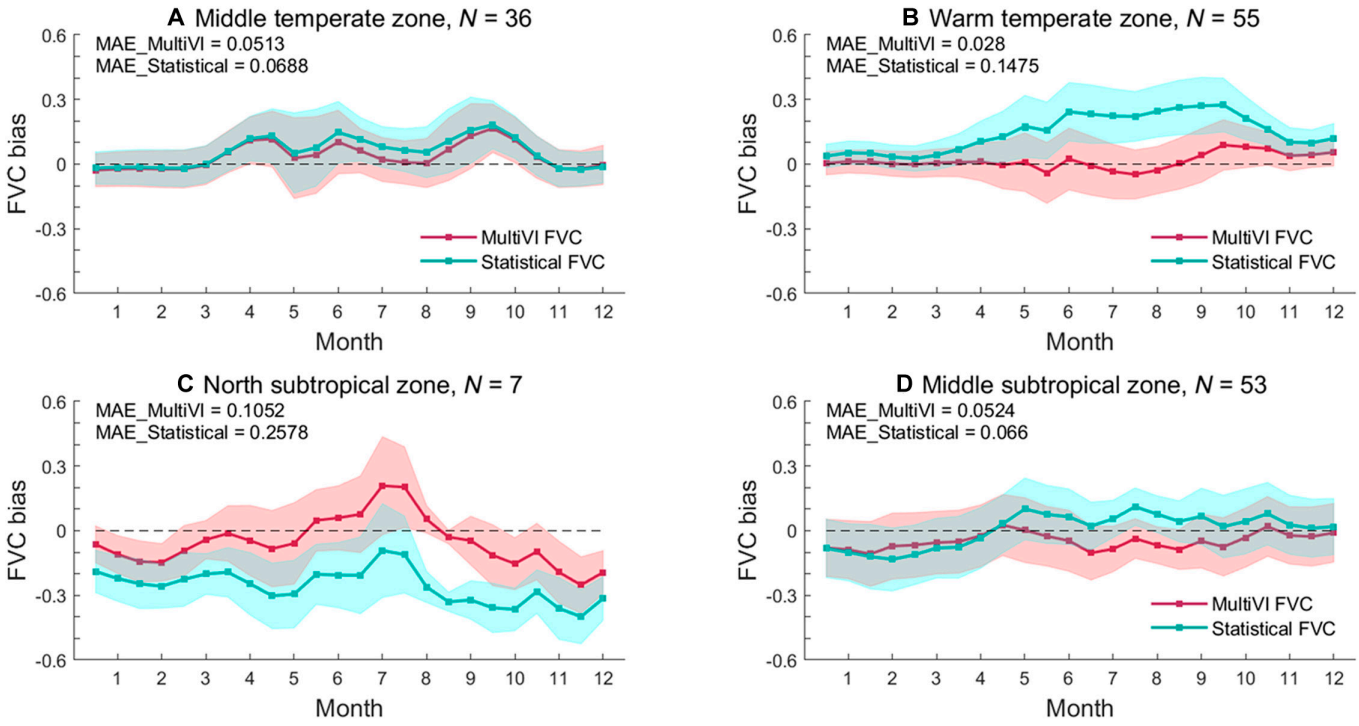

Fig. 13. (A to D) Average bias of the MultiVI FVC and the Statistical FVC versus the field-measured FVC over the time series FVC monitoring plots for each temporal phase and ecological and geographical zone in 2010. The mean absolute errors (MAEs) for the 24 time phases are also shown. The width of the shading represents ±1 standard deviation.

when compared to the field-measured FVC. However, the Statistical FVC demonstrated significantly higher overestimation ($RMSD_S = 0.2561$) compared to the MultiVI FVC ($RMSD_M = 0.0742$). The largest discrepancy (close to 0.3) between the MultiVI FVC and field-measured FVC occurred in summer (June or July) over the mountainous croplands (Fig. 12K and L). For the croplands in the plains (Fig. 12G and H), the MultiVI FVC exhibited relatively high accuracy compared to those of the croplands on mountainous and hilly terrain (Fig. 12I to L).

The 151 plots were categorized according to the Chinese ecological and geographical zoning classification. Figure 13 illustrates the average bias between the MultiVI FVC and the field-measured FVC, as well as between the Statistical FVC and the field-measured FVC over 151 plots for ecological and geographical zones in 2010. In the middle temperate zone (Fig. 13A), both the MultiVI FVC and the Statistical FVC exhibited a general trend of overestimation compared to the field-measured FVC, especially in April and September, with biases of approximately 0.1. The bias of the MultiVI FVC was significantly lower than that of the Statistical FVC in the warm temperate zone (Fig. 13B) and the north subtropical zone (Fig. 13C), with the mean absolute error (MAE) being more than 0.1 lower. In the warm temperate zone, the Statistical FVC tended to overestimate the results, while in the north subtropical zone, it underestimated them by up to 0.3 compared to the field-measured FVC. In the middle subtropical zone (Fig. 13D), the MultiVI FVC was slightly underestimated compared to the field-measured FVC, particularly from June to September.

Discussion

The accuracy of the endmember NDVI values influenced the performance of the FVC derived using the VI-based mixture model. The *Vv* and *Vs* values are usually obtained using statistical methods based on remotely sensed images. However, the statistical criteria are hard to define for different areas since their climatology and vegetation biomes vary. Inappropriate statistical endmembers can introduce significant errors in FVC estimation. The underestimation of the *Vs* results in an overestimation of FVC, with errors reaching 0.2 in grassland and shrubland areas [64]. This study introduced a novel framework for developing high-resolution FVC products over a large scale by applying the *Vv* and *Vs* values derived from MODIS data using the MultiVI algorithm to Landsat images. The 500-m endmembers were downscaled to 30 m based on the land cover dataset for further synergistic applications [29]. Song et al. demonstrated that downscaling of *Vv* and *Vs* significantly improved the accuracy of FVC estimation since the land cover types influenced the spatial heterogeneity within the endmember at a 500-m resolution [29]. The validation and analysis demonstrated that the MultiVI FVC outperformed the FVC derived using statistical endmembers, with lower RMSD (Fig. 12) and bias (Fig. 13) values compared to the field-measured FVC. Figure 13B and C shows large uncertainties in the Statistical FVC due to the absence of suitable *Vv* and *Vs* values for warm temperate and subtropical zones, respectively. GLASS FVC and GEOV3 FVC typically employ machine learning methods and physical models. Due to its simplicity and practicability, the VI-based mixture model for FVC estimation is easier to use and more flexible than machine learning methods. However, challenges in obtaining accurate *Vv* and *Vs* values limit its accuracy. The performance of the MultiVI FVC demonstrated that the VI-based mixture model incorporated with the MultiVI method improved the quality of FVC compared to the traditional VI-based mixture model. Additionally, the generation of the MultiVI FVC was not restricted by the data source or study area and could be applied to other satellite datasets with different resolutions, such as Sentinel, ZY-3, and GF-1 datasets, if the *Vv* and *Vs* maps are calculated in advance [29].

Spatially complete, high-frequency satellite time series data are essential for generating easy-to-use FVC products. Due to the limited revisit cycle of the Landsat satellites, cloud contamination, and cloud shadow, data fusion is required to provide a spatially continuous 30-m/15-day dataset with good quality. Various methods have been developed to fill the gaps in Landsat images. Commonly used approaches fuse the daily revisit MODIS data with Landsat data to generate a dataset with both fine spatial and high temporal resolutions [66–68]. However, these models usually employ weighted sum functions and moving windows to construct synthetic fusion data from Landsat and MODIS images. They have relatively high computational costs. Moreover, the prediction accuracy of these models is always sensitive to land heterogeneity and becomes less reliable when land surface changes occur at finer scales than that of the MODIS dataset [69,70]. In comparison to these methods, the harmonic models applied in this study are free of complicated neighbor calculations and are more suitable for implementation on GEE at a large scale. Three types of harmonic models with different numbers of coefficients, i.e., the simple, advanced, and full versions, were automatically selected according to the amount of Landsat data available. Due to this data-adaptive flexibility of the harmonic model, it is feasible to use Landsat data to produce a 30-resolution semimonthly FVC at the regional or continental scale. More types of Landsat-like satellite data, e.g., Sentinel-2, can be efficiently adopted in this framework.

The MultiVI FVC had consistent spatial and temporal patterns with the other popular products, i.e., the GLASS FVC and the GEOV3 FVC (Figs. 8 to 11). Overall, the MultiVI FVC values were lower than the GEOV3 FVC and higher than the GLASS FVC. The validation of the GEOV3 products demonstrated that the scale factor employed in CYCLOPES fCOVER to derive the GEOV FVC product might be too high, which results in overestimation [51]. Figure 8 shows that the MultiVI FVC values were slightly higher than the GLASS FVC over grasslands and lower over deciduous forests. The spatiotemporal comparison and validation of global-scale GLASS FVC with the GEOV FVC products also illustrated that the GLASS FVC had more pixels with low values close to 0 for grasslands and slightly higher values compared to the GEOV2 product over deciduous forests [71]. The uncertainty of the FVC estimation was below 0.1 for the Huailai and Saihanba sites in this study, which was comparable to the GLASS FVC but higher than the accuracy of GEOV3 (Fig. 11).

The uncertainty of the MultiVI FVC and the discrepancies between the three FVC products appeared to be relatively high for humid areas such as paddy rice fields (Fig. 9) and tropical zones with evergreen forests (Fig. 10A and B), which were indicated to have accuracy problems according to the validation report of the GEOV3 product [51]. The evergreen forest areas in the tropical zone have year-round cloud coverage as well as rainy climates, which result in large data gaps in these areas. The lower data availability introduces greater uncertainties to the harmonic time series models and results in lower precision of the FVC derivation. Figure 10D and H demonstrates that the MultiVI FVC showed zero values during winter, which was correlated with the snow-covered surface. The MultiVI FVC should be used with caution in these areas since it was derived from optical remotely sensed imageries and cannot reflect the coverage status of the vegetation under snow. Since the MultiVI FVC was derived from the NDVI time series, it was affected by background effects. The water bodies and wet soil background might weaken the reflectance of vegetation, especially in the NIR band [64,72]. The anisotropy of the vegetation canopy is also weakened and might introduce greater uncertainty in the MultiVI method using multiangle data to derive the endmember NDVI values of the VI-based mixture model. Additionally, other weaknesses of remote sensing reflectance and NDVI methods, such as topographic effects, may also be directly reflected in the FVC products, which may explain the lower accuracy in mountainous and hilly terrain in Fig. 12.

Conclusion

In this study, a pragmatic method was proposed for generating 30-m/15-day FVC products based on the GEE platform. An improved VI-based mixture model was used to derive the FVC products from 2010 to 2020. The MultiVI algorithm was applied to generate the endmember maps of the VI-based mixture model at a 30-m resolution over China. The harmonic temporal interpolation method was subsequently employed to generate a spatially continuous 30-m/15-day NDVI. The MultiVI FVC products had a fine spatial resolution (30 m) and a semimonthly frequency. Therefore, these products could facilitate the monitoring of vegetation dynamics at a finer resolution compared to kilometer-level products. The quality and accuracy of the MultiVI FVC products were evaluated using other published FVC products and ground-measured datasets. The comparison with the GLASS FVC and the GEOV3 FVC products demonstrated that the three products generally had similar spatial patterns and temporal trajectories, with RMSD values close to 0.1 and R^2 values of approximately 0.8 (Figs. 9 and 10) in most areas of China. Relatively large discrepancies appeared in the tropical evergreen forest and paddy rice field areas. Direct validation with extensive vegetation biomes of croplands, forests, and grasslands and field-measured FVC time series datasets was also conducted. The accuracy of the MultiVI FVC against the field-measured FVC was reasonable (RMSD = 0.0906 for the Huailai site and RMSD = 0.0951 for the Saihanba site). The MultiVI FVC showed similar temporal trajectories to the field-measured FVC time series in the 22 small watersheds, with RMSD values below 0.1 and R^2 values reaching 0.9 for most vegetation types. Uncertainty was found in areas with complicated land surfaces, such as flooded paddy fields and hilly rainfed croplands. The enhanced VI-based mixture model improved the accuracy of FVC estimation compared to the traditional VI-based mixture model using statistical endmembers. The developed operational framework in this study showed practicability and flexibility in deriving fine-resolution and high-frequency FVC products at large scales with maps of endmember VIs.

Acknowledgments

The field-measured dataset at the Saihanba site was provided by the Chengde Remote Sensing Test Site, State Key Laboratory of Remote Sensing Sciences.

Funding: This research was financially supported by the National Natural Science Foundation of China (grant nos. 42090013, 42271338, and 41871230).

Author contributions: X.M. led the research and revised the manuscript. T.Z. produced and validated the FVC. W.S. contributed to part of the coding work. Y.L. helped with the collection and analysis of the field-measured data. G.Y., Y.X., and D.X. guided the research and helped improve the manuscript. B.Z. and L.J. processed the necessary auxiliary data.

Competing interests: The authors declare that they have no competing interests.

Data Availability

The dataset will be available at https://data.tpdc.ac.cn/home.

References

1. Deardorff JW. Efficient prediction of ground surface-temperature and moisture, with inclusion of a layer of vegetation. *J Geophys Res Oceans*. 1978;83(C4):1889–1903.
2. Hirano Y, Yasuoka Y, Ichinose T. Urban climate simulation by incorporating satellite-derived vegetation cover distribution into a mesoscale meteorological model.` *Theor Appl Climatol*. 2004;79(3-4):175–184.
3. Eriksson HM, Eklundh L, Kuusk A, Nilson T. Impact of understory vegetation on forest canopy reflectance and remotely sensed LAI estimates. *Remote Sens Environ*. 2006;103(4):408–418.
4. Arneth A. Uncertain future for vegetation cover. *Nature*. 2015;524(7563):44–45.
5. Xie M, Wang Y, Meichen FU. An overview and perspective about causative factors of surface urban heat island effects. *Prog Geogr*. 2011;30(1):35–41.
6. Naqvi HR, Mallick J, Devi LM, Siddiqui MA. Multi-temporal annual soil loss risk mapping employing revised universal soil loss equation (RUSLE) model in Nun Nadi Watershed, Uttrakhand (India). *Arab J Geosci*. 2013;6(10):4045–4056.
7. Gan M, Deng J, Zheng X, Hong Y, Wang K. Monitoring urban greenness dynamics using multiple endmember spectral mixture analysis. *PLoS One*. 2014;9(11):Article e112202.
8. Li X, Zhang X, Zhang L, Wu B. Rainfall and vegetation coupling index for soil erosion risk mapping. *J Soil Water Conserv*. 2014;69(3):213–220.
9. Zhang Y, Odeh I, Ramadan E. Assessment of land surface temperature in relation to landscape metrics and fractional vegetation cover in an urban/peri-urban region using Landsat data. *Int J Remote Sens*. 2013;34(1-2):168–189.
10. Fernández-Guisuraga JM, Verrelst J, Calvo L, Suárez-Seoane S. Hybrid inversion of radiative transfer models based on high spatial resolution satellite reflectance data improves fractional vegetation cover retrieval in heterogeneous ecological systems after fire. *Remote Sens Environ*. 2021;255:112304.
11. Mu X, Zhao T, Ruan G, Song J, Wang J, Yan G, Mcvicar TR, Yan K, Gao Z, Liu Y. High spatial resolution and high temporal frequency (30-m/15-day) fractional vegetation cover estimation over China using multiple remote sensing datasets: Method development and validation. *J Meteorol Res*. 2021;35(1):128–147.
12. Tao G, Jia K, Zhao X, Wei X, Xie X, Zhang X, Wang B, Yao Y, Zhang X. Generating high spatio-temporal resolution fractional vegetation cover by fusing GF-1 WFV and MODIS data. *Remote Sens*. 2019;11(19):2324.
13. Song DX, Wang Z, He T, Wang H, Liang S. Estimation and validation of 30 m fractional vegetation cover over China through integrated use of Landsat 8 and Gaofen 2 data. *Sci Remote Sens*. 2022;6:Article 100058.
14. White MA, Nemani RR, Thornton PE, Running SW. Satellite evidence of phenological differences between urbanized and rural areas of the eastern United States deciduous broadleaf forest. *Ecosystems*. 2002;5(3):260–273.
15. Johnson LF, Trout TJ. Satellite NDVI assisted monitoring of vegetable crop evapotranspiration in California's San Joaquin Valley. *Remote Sens*. 2012;4(2):439–455.
16. Hansen MC, Potapov PV, Moore R, Hancher M, Turubanova SA, Tyukavina A, Thau D, Stehman SV, Goetz SJ, Loveland TR, et al. High-resolution global maps of 21st-century forest cover change. *Science*. 2013;342(6160):850–853.
17. Zhang X, Long T, He G, Guo Y. Gobal forest cover mapping using Landsat and Google Earth Engine cloud computing. In: *2019 8th International Conference on Agro-Geoinformatics (Agro-Geoinformatics)*. Istanbul (Turkey): IEEE; 2019. p. 1-5.
18. Kim D, Sexton J, Noojipady P, Huang C, Channan S, Townshend J. Global forest cover change assessment from 1990s to 2000s at 30m. In: *AGU Fall Meeting Abstracts*. California (USA): American Geophysical Union; 2013. p. B43C-0501.
19. Liu B, Zhang K, Xie Y. An empirical soil loss equation. In: *12th International Soil Conservation Organization Conference*. Beijing (China). 12th ISCO Conference; 2002. p. 26–31.
20. Gutman G, Ignatov A. The derivation of the green vegetation fraction from NOAA/AVHRR data for use in numerical weather prediction models. *Int J Remote Sens*. 1998;19(8):1533–1543.
21. Roujean J-L, Lacaze R. Global mapping of vegetation parameters from POLDER multiangular measurements for studies of surface-atmosphere interactions: A pragmatic method and its validation. *J Geophys Res Atmos*. 2002;107(D12):ACL 6-1–ACL 6-14.
22. Baret F, Hagolle O, Geiger B, Bicheron P, Miras B, Huc M, Berthelot B, Niño F, Weiss M, Samain O, et al. LAI, fAPAR and fCover CYCLOPES global products derived from VEGETATION: Part 1: Principles of the algorithm. *Remote Sens Environ*. 2007;110(3):275–286.
23. Xiao Z, Wang T, Liang S, Sun R. Estimating the fractional vegetation cover from GLASS leaf area index product. *Remote Sens*. 2016;8(4):337.
24. Gao L, Wang X, Johnson BA, Tian Q, Wang Y, Verrelst J, Mu X, Gu X. Remote sensing algorithms for estimation of fractional vegetation cover using pure vegetation index values: A review. *ISPRS J Photogramm Remote Sens*. 2020;159:364–377.
25. Zhang X, Liao C, Li J, Su Q. Fractional vegetation cover estimation in arid and semi-arid environments using HJ-1 satellite hyperspectral data. *Int J Appl Earth Obs Geoinf*. 2013;21:506–512.
26. Jiapaer G, Chen X, Bao A. A comparison of methods for estimating fractional vegetation cover in arid regions. *Agric For Meteorol*. 2011;151(12):1698–1710.
27. Song W, Mu X, Ruan G, Gao Z, Li L, Yan G. Estimating fractional vegetation cover and the vegetation index of bare soil and highly dense vegetation with a physically based method. *Int J Appl Earth Obs Geoinf*. 2017;58:168–176.
28. Mu X, Song W, Zhan G, Mcvicar TR, Donohue RJ, Yan G. Fractional vegetation cover estimation by using multi-angle vegetation index. *Remote Sens Environ*. 2018;216:44–56.
29. Song W, Zhao T, Mu X, Zhong B, Zhao J, Yan G, Wang L, Niu Z. Using a vegetation index-based mixture model to estimate fractional vegetation cover products by jointly using multiple satellite data: Method and feasibility analysis. *Forests*. 2022;13(5):691.
30. Jia K, Liang S, Liu S, Li Y, Xiao Z, Yao Y, Jiang B, Zhao X, Wang X, Xu S. Global land surface fractional vegetation cover estimation using general regression neural networks from

MODIS surface reflectance. *IEEE Trans Geosci Remote Sens*. 2015;53(9):4787–4796.
31. Yang L, Jia K, Liang S, Liu J, Wang X. Comparison of four machine learning methods for generating the GLASS fractional vegetation cover product from MODIS data. *Remote Sens*. 2016;8(8):682.
32. Baret F, Weiss M, Verger A. ATBD for LAI, FAPAR and FCOVER from Proba-v products at 300m resolution (GEOV3) (ATBD). ImagineS_RP2.1_ATBD-LAI300M France; 2016; 1.73.
33. Zhang X, Liu L, Chen X, Gao Y, Mi J. GLC_FCS30: Global land-cover product with fine classification system at 30 m using time-series Landsat imagery. *Earth Syst Sci Data*. 2020;13(6):2753-2776.
34. Baret F, Morissette JT, Fernandes RA, Champeaux J, Myneni RB, Chen J, Plummer S, Weiss M, Bacour C, Garrigues S. Evaluation of the representativeness of networks of sites for the global validation and intercomparison of land biophysical products: Proposition of the CEOS-BELMANIP. *IEEE Trans Geosci Remote Sens*. 2006;44(7):1794–1803.
35. Mu X, Huang S, Chen Y. HiWATER: Dataset of fractional vegetation cover in the middle reaches of the Heihe River Basin. Beijing (China): Beijing Normal University; 2013.
36. Li X, Liu S, Ma M, Xiao Q, Liu Q, Jin R, Che T, Wang W, Qi Y, Li H, et al. HiWATER: An integrated remote sensing experiment on hydrological and ecological processes in the Heihe River Basin. *Adv Earth Science*. 2012;27(5):481–498.
37. Song W, Mu X, Yan G, Huang S. Extracting the green fractional vegetation cover from digital images using a shadow-resistant algorithm (SHAR-LABFVC). *Remote Sens*. 2015;7(8):10425–10443.
38. Yan G, Mu X, Liu Y. Fractional vegetation cover. In: Liang S, Li X, Wang J, editors. *Advanced remote sensing*. Boston: Academic Press; 2012. p. 415 –438.
39. Zhang W, Lu B, Shi W. Determination of vegetation coverage by photograph and automatic calculation. *Bull Soil Water Conserv*. 2009;29(002):39–42.
40. Mu X, Huang S, Ren H, Yan G, Song W, Ruan G. Validating GEOV1 fractional vegetation cover derived from coarse-resolution remote sensing images over croplands. *IEEE J Sel Top Appl Earth Obs Remote Sens*. 2014;8(2):439–446.
41. Xiao J, Moody A. A comparison of methods for estimating fractional green vegetation cover within a desert-to-upland transition zone in Central New Mexico, USA. *Remote Sens Environ*. 2005;98(2-3):237–250.
42. Li F, Kustas WP, Prueger JH, Neale CM, Jackson TJ. Utility of remote sensing–based two-source energy balance model under low-and high-vegetation cover conditions. *J Hydrometeorol*. 2005;6(6):878–891.
43. Yang A, Zhong B, Lv W, Wu S, Liu Q. Cross-calibration of GF-1/WFV over a desert site using Landsat-8/OLI imagery and ZY-3/TLC data. *Remote Sens*. 2015;7(8):10763–10787.
44. Zhong B, Wu S, Yang A, Liu Q. An improved aerosol optical depth retrieval algorithm for moderate to high spatial resolution optical remotely sensed imagery. *Remote Sens*. 2017;9(6):555.
45. Roy DP, Kovalskyy V, Zhang HK, Vermote EF, Yan L, Kumar SS, Egorov A. Characterization of Landsat-7 to Landsat-8 reflective wavelength and normalized difference vegetation index continuity. *Remote Sens Environ*. 2016;185:57–70.
46. Foga S, Scaramuzza PL, Guo S, Zhu Z, Dilley RD Jr, Beckmann T, Schmidt GL, Dwyer JL, Hughes MJ, Laue B. Cloud detection algorithm comparison and validation for operational Landsat data products. *Remote Sens Environ*. 2017;194:379–390.
47. Roujean J-L, Leroy M, Deschamps P-Y. A bidirectional reflectance model of the Earth's surface for the correction of remote sensing data. *J Geophys Res Atmos*. 1992;97(D18):20455–20468.
48. Schaaf CB, Gao F, Strahler AH, Lucht W, Li X, Tsang T, Strugnell NC, Zhang X, Jin Y, Muller J-P. First operational BRDF, albedo nadir reflectance products from MODIS. *Remote Sens Environ*. 2002;83(1-2):135–148.
49. Jia K, Yang L, Liang S, Xiao Z, Zhao X, Yao Y, Zhang X, Jiang B, Liu D. Long-term global land surface satellite (GLASS) fractional vegetation cover product derived from MODIS and AVHRR data. *IEEE J Sel Top Appl Earth Obs Remote Sens*. 2018;12(2):508–518.
50. Jia K, Liang S, Wei X, Yao Y, Yang L, Zhang X, Liu D. Validation of global LAnd surface satellite (GLASS) fractional vegetation cover product from MODIS data in an agricultural region. *Sens Lett*. 2018;9(9):847–856.
51. Fuster B, Camacho F, Verger A, Lacaze R, Weiss M, Baret F, Smets B. Quality assessment of PROBA-V LAI, fAPAR and fCOVER collection 300 m products of Copernicus global land service. *Remote Sens*. 2020;12(6):1017.
52. Gitelson AA, Kaufman YJ, Stark R, Rundquist D. Novel algorithms for remote estimation of vegetation fraction. *Remote Sens Environ*. 2002;80(1):76–87.
53. Nilson T. A theoretical analysis of the frequency of gaps in plant stands. *Agric Meteorol*. 1971;8:25–38.
54. Goel NS, Strebel DE. Simple Beta distribution representation of leaf orientation in vegetation canopies. *Agron J*. 1984;76(5):800–802.
55. Choudhury BJ, Ahmed NU, Idso SB, Reginato RJ, Daughtry C. Relations between evaporation coefficients and vegetation indices studied by model simulations. *Remote Sens Environ*. 1994;50(1):1–17.
56. Leblanc SG, Chen JM, Miller JR, Freemantle J. Compact airborne spectrographic imager (CASI) used for mapping LAI of cropland. *J Geophys Res Atmos*. 1999;104(D22): 27945–27958.
57. He L, Chen JM, Pisek J, Schaaf C, Strahler AH. Global clumping index map derived from the MODIS BRDF product. *Remote Sens Environ*. 2012;119:118–130.
58. Roujean JL, Leroy PM, Deschamps Y. A bidirectional reflectance model of the Earth's surface for the correction of remote sensing data. *J Geophys Res*. 1992;97(D18):20455–20468.
59. Chen J, Liao A, Chen J, Peng S, Chen L, Zhang H. 30-meter global land cover data product- globe Land30. *Geomatics World*. 2017;24(1):1–8.
60. Zeng X, Dickinson RE, Walker A, Shaikh M, DeFries RS, Qi J. Derivation and evaluation of global 1-km fractional vegetation cover data for land modeling. *J Appl Meteorol*. 2000;39(6):826–839.
61. Zhu Z, Woodcock CE, Holden C, Yang Z. Generating synthetic Landsat images based on all available Landsat data: Predicting Landsat surface reflectance at any given time. *Remote Sens Environ*. 2015;162:67–83.
62. Zhe Z, Woodcock CE. Continuous change detection and classification of land cover using all available Landsat data. *Remote Sens Environ*. 2013;144:152–171.
63. Weiss M, Baret F, Garrigues S, Lacaze R. LAI and fAPAR CYCLOPES global products derived from VEGETATION.

Part 2: Validation and comparison with MODIS collection 4 products. *Remote Sens Environ*. 2007;110(3):317–331.
64. Montandon LM, Small EE. The impact of soil reflectance on the quantification of the green vegetation fraction from NDVI. Remote Sens Environ. 2008;112(4):1835-1845.
65. Adam E, Mutanga O, Rugege D. Multispectral and hyperspectral remote sensing for identification and mapping of wetland vegetation: A review. *Wetl Ecol Manag*. 2010;18(3):281–296.
66. Gao F, Masek J, Schwaller M, Hall F. On the blending of the Landsat and MODIS surface reflectance: Predicting daily Landsat surface reflectance. *IEEE Trans Geosci Remote Sens*. 2006;44(8):2207–2218.
67. Zhu X, Chen J, Gao F, Chen X, Masek JG. An enhanced spatial and temporal adaptive reflectance fusion model for complex heterogeneous regions. *Remote Sens Environ*. 2010;114(11):2610–2623.
68. Roy DP, Ju J, Lewis P, Schaaf C, Gao F, Hansen M, Lindquist E. Multi-temporal MODIS–Landsat data fusion for relative radiometric normalization, gap filling, and prediction of Landsat data. *Remote Sens Environ*. 2008;112(6):3112–3130.
69. Yan L, Roy DP. Spatially and temporally complete Landsat reflectance time series modelling: The fill-and-fit approach. *Remote Sens Environ*. 2020;241:Article 111718.
70. Chen B, Huang B, Xu B. Comparison of spatiotemporal fusion models: A review. *Remote Sens*. 2015;7(2):1798–1835.
71. Liu D, Jia K, Wei X, Xia M, Zhang X, Wang B. Spatiotemporal comparison and validation of three global-scale fractional vegetation cover products. *Remote Sens*. 2019;11(21):2524.
72. Luo S, Wang C, Pan F, Xi X, Li G, Nie S, Xia S. Estimation of wetland vegetation height and leaf area index using airborne laser scanning data. *Ecol Indic*. 2015;48:550–559.
73. Lacaze R, Richaume P, Hautecoeur O, Lalanne T, Quesney A, Maignan F, Bicheron P, Leroy M, Breon FM. Advanced algorithms of the ADEOS-2/POLDER-2 land surface process line: Application to the ADEOS-1/POLDER-1 data. *IGARSS 2003*. 2003;7992521.
74. García-Haro FJ, Camacho de Coca F, Meliá J, Martinez B. Operational derivation of vegetation products in the framework of the LSA SAF project. Paper presented at: the EUMETSAT Meteorological Satellite Conference; 2005; Dubrovnik, Croatia.
75. García-Haro FJ, Sommer S, Kemper T. A new tool for variable multiple endmember spectral mixture analysis (VMESMA). *Int J Remote Sens*. 2005;26(10):2135–2162.
76. Bacour C, Baret F, Béal D, Weiss M, Pavageau K. Neural network estimation of *LAI*, *fAPAR*, *fCover* and $LAI \times C_{ab}$, from top of canopy MERIS reflectance data: Principles and validation. *Remote Sens Environ*. 2006;105(4):313–325.
77. Baret F, Weiss M, Lacaze R, Camacho F, Makhmara H, Pacholcyzk P, Smets B. GEOV1: *LAI* and *FAPAR* essential climate variables and *FCOVER* global time series capitalizing over existing products. Part1: Principles of development and production. *Remote Sens Environ*. 2013;137:299–309.
78. Mu X, Liu Q, Ruan G, Zhao J, Zhong B, Wu S, Peng JJ. A 1 km/5 day fractional vegetation cover dataset over China-ASEAN (2013). *J Glob Change Data Discov*. 2017;1:45–51.

Journal of Remote Sensing
A SCIENCE PARTNER JOURNAL

Mapping Spatially Seamless Fractional Vegetation Cover over China at a 30-m Resolution and Semimonthly Intervals in 2010–2020 Based on Google Earth Engine

Tian Zhao, Xihan Mu, Wanjuan Song, Yaokai Liu, Yun Xie, Bo Zhong, Donghui Xie, Lingmei Jiang, and Guangjian Yan

Citation: Zhao T, Mu X, Song W, Liu Y, Xie Y, Zhong B, Xie D, Jiang L, Yan G. Mapping Spatially Seamless Fractional Vegetation Cover over China at a 30-m Resolution and Semimonthly Intervals in 2010–2020 Based on Google Earth Engine. *J Remote Sens*. 2023;**3**:0101. DOI: 10.34133/remotesensing.0101

Fractional vegetation cover (FVC) is a critical biophysical parameter that characterizes the status of terrestrial ecosystems. The spatial resolutions of most existing FVC products are still at the kilometer level. However, there is growing demand for FVC products with high spatial and temporal resolutions in remote sensing applications. This study developed an operational method to generate 30-m/15-day FVC products over China. Landsat datasets were employed to generate a continuous normalized difference vegetation index (NDVI) time series based on the Google Earth Engine platform from 2010 to 2020. The NDVI was transformed to FVC using an improved vegetation index (VI)-based mixture model, which quantitatively calculated the pixelwise coefficients to transform the NDVI to FVC. A comparison between the generated FVC, the Global LAnd Surface Satellite (GLASS) FVC, and a global FVC product (GEOV3 FVC) indicated consistent spatial patterns and temporal profiles, with a root mean square deviation (RMSD) value near 0.1 and an $R2$ value of approximately 0.8. Direct validation was conducted using ground measurements from croplands at the Huailai site and forests at the Saihanba site. Additionally, validation was performed with the FVC time series data observed at 151 plots in 22 small watersheds. The generated FVC showed a reasonable accuracy (RMSD values of less than 0.10 for the Huailai and Saihanba sites) and temporal trajectories that were similar to the field-measured FVC (RMSD values below 0.1 and $R2$ values of approximately 0.9 for most small watersheds). The proposed method outperformed the traditional VI-based mixture model and had the practicability and flexibility to generate the FVC at different resolutions and at a large scale.
Image